General Disclaimer

One or more of the Following Statements may affect this Document

- This document has been reproduced from the best copy furnished by the organizational source. It is being released in the interest of making available as much information as possible.

- This document may contain data, which exceeds the sheet parameters. It was furnished in this condition by the organizational source and is the best copy available.

- This document may contain tone-on-tone or color graphs, charts and/or pictures, which have been reproduced in black and white.

- This document is paginated as submitted by the original source.

- Portions of this document are not fully legible due to the historical nature of some of the material. However, it is the best reproduction available from the original submission.

Produced by the NASA Center for Aerospace Information (CASI)

DRA

Georgia Institute of Technology
A UNIT OF THE UNIVERSITY SYSTEM OF GEORGIA
ATLANTA GEORGIA 30332

(NASA-CR-174609) A VISCOUS-INVISCID INTERACTIVE PROCEDURE FOR ROTATIONAL FLOW IN CASCADES OF TWO DIMENSIONAL AIRFOILS OF ARBITRARY SHAPE Final Report, 15 Mar. 1979 - 13 Aug. 1982 (Georgia Inst. of Tech.) G3/02

N84-13149

Unclas
15089

Final Report
Project Director: Dr. William A. Johnston
Grant No. NSG-3260
" A Viscuous-Inviscid Interactive Procedure for Rotational Flow in Cascades of Two Dimensional Airfoils of Arbitrary Shape "
period covered: 3/15/79-8/13/82

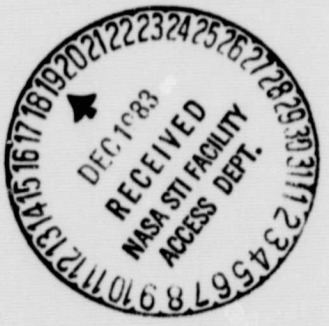

TABLE OF CONTENTS

		Page No.
SUMMARY		1
I.	INTRODUCTION	2
II.	GRID GENERATION	4
III.	THE INVISCID SOLUTION	13
	Boundary Conditions	15
IV.	THE VISCOUS SOLUTION AND INTERACTIVE PROCEDURE	19
	Governing Equations	20
	Grid Mesh for the Marching Calculation	24
	The Numerical Scheme	24
	Additional Computational Features	26
	The Interactive Procedure	27
V.	NUMERICAL RESULTS AND DISCUSSION	29
	Unstaggered Cascade (NACA 0012 blades)	29
	45° Staggered Cascade (NACA 65-410 blades)	41
	28.5° Staggered Cascade (NACA 65-(12)10 blades)	47
	Discussion	57
	REFERENCES	61

SUMMARY

A viscous-inviscid interactive calculation procedure is developed for application to flow in cascades of two-dimensional airfoils. This procedure has essentially three components. First, a numerical solution of the Euler equations which can accommodate an arbitarily specified cascade geometry is carried out on a nonorthogonal curvilinear grid mesh that is fitted to the geometry of the cascade. A method of grid generation has been used which relies in part on a succession of conformal mappings. Second, a viscous solution for use in boundary layer and wake regions has been programmed. Finally, an interactive scheme which takes the form of a source-sink distribution along the blade surface and wake centerline is employed. Results have been obtained with this procedure for several cascade flow situations, and some comparisons with experiment are presented.

I. INTRODUCTION

In recent years, a great deal of progress has been made in the development of faster, more efficient numerical procedures for the calculation of flow past aerodynamic shapes. Algorithms for the solution of the Euler equations and Navier-Stokes equations have been available for some time; for example, MacCormack's Method [1], an explicit time marching procedure, has been widely used since its introduction in 1969. More recently, time marching algorithms which have an implicit [2-4] or hybrid [5] character have been introduced. These implicit methods are not subject to the severe stability restrictions which explicit methods experience, and are therefore less time consuming.

In addition to the need for an efficient flow calculation algorithm, another requirement in aerodynamic calculations is some technique for dealing with the complex geometries that often occur. Several different grid generation schemes have been developed in recent years to meet this requirement. Certainly among the most popular of these is a versatile method for dealing with aerodynamic geometries developed by Thompson, Thames, and Mastin [6, 7]. In this method, which has been used in calculating the flow about isolated airfoils as well as other aerodynamic shapes, a non-orthogonal curvilinear grid mesh having a grid line coincident with the airfoil surface is generated by the solution of a system of elliptic partial differential equations. The coordinate transformation used in this method coresponds to the mapping of a region which encloses the airfoil in the physical plane, onto a region which is the interior of a rectangle in the computational plane. Steger [8] has combined the Beam and Warming implicit finite difference algorithm [4] with

the grid generation procedure of Thompson et al, to simulate compressible flow about isolated airfoils.

While similar in many respects to flow calculations for isolated airfoils, flow calculations for cascades encounter some additional difficulties in terms of the geometry and the boundary conditions which must be applied. The necessity for dealing effectively with complicated geometries in cascade flow problems has led to the development of several diverse geometry procedures (see for example [9-12]). Recently, Steger et al [13] have applied the approach used by Steger in the isolated airfoil problem to flow through cascades.

In the present research effort, a body fitted nearly orthogonal curvilinear grid is generated by a method which relies in part on a succession of conform mappings. This is described in Section II. An implicit time marching finite difference solution of the Euler equations is then carried out on this grid in the manner described in References [8,13], except for certain differences in the treatment of boundary conditions. The inviscid flow solution is discussed in Section III. In the present research effort, we have accounted for the effect of viscosity on the flow by coupling the inviscid calculation with a separate viscous shear layer calculation. This viscous calculation, which consists of a marching finite difference calculation for turbulent flow, is initiated at the stagnation point and proceeds through the blade boundary layers and into the blade wake. We have attempted to assess the economy of including viscous effects within the calculation in this manner, relative to the Navier-Stokes approach of Reference [13].

ORIGINAL PAGE IS
OF POOR QUALITY

II. GRID GENERATION

The inviscid computations of the present work are performed on a C-type body-fitted grid in which one family of lines forms open loops (C's) around the blade and wake. The grid is periodic and nearly orthogonal. This choice permits accurate resolution of the leading edge region and provides an appropriate location for the interactive wake boundary conditions to be described later.

The grid generation employs two analytical mappings which take the multiply-connected exterior of a cascade of airfoils to the interior of a simply connected domain. A numerically constructed mapping is then used to take this into a rectangular computational space. The first mapping transforms the exterior of a staggered cascade of semi-infinite flat plates in the z-plane into the interior of the unit circle in the w-plane.

$$z = z_0 + \lambda\left[e^{-i\gamma}(\log w - i\pi) - 2\cos\gamma \log(1-w)\right] \qquad (2\text{-}1)$$

where γ is the stagger angle, s is the pitch, and $\lambda = (s/2\pi)\exp(i\gamma)$. This form is obtained from the standard mapping for a cascade of finite flat plates [14] by moving the singularities to 0 and +1 in the w-plane. At the leading edge z_1 of the central plate $dz/dw = 0$. Solving for w_1 and substituting into Eq. (2-1) gives

$$z_0 = z_1 + 2\lambda\left[\gamma\sin\gamma + \cos\gamma \log(2\cos\gamma)\right] \qquad (2\text{-}2)$$

When this mapping is applied to a real geometry, such as the turbine cascade in Figure 1, the flat plate is taken to run from a point just inside the leading edge through the downstream end of the wake.

The second mapping transforms the interior of the unit circle in the w-plane, with a branch cut from 0 to +1 along the real axis, to the interior of the infinite strip between the real axis and $-i\pi/2$ in the ζ-plane.

ORIGINAL PAGE IS
OF POOR QUALITY

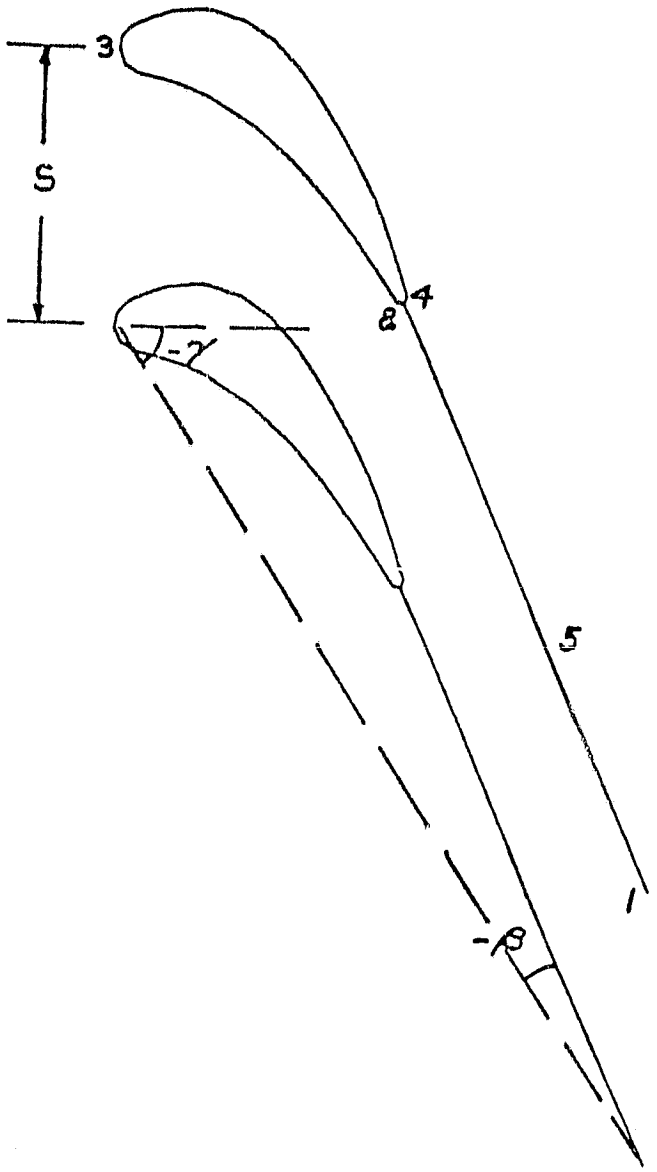

Figure 1. Turbine Cascade with Mapping Nomenclature in z-Plane.

OF POOR QUALITY

$$w = \tanh^2(\zeta/2) \tag{2-3}$$

Note that reflection of ζ through the origin leaves w unchanged. This will be used later as a convenient means for analytical continuation. The image of the turbine cascade and straight wakes in the ζ-plane (Figure 2) is a pair of parallel straight lines connected by a roughly s-shaped curve. Note the locations of corresponding points 1 to 5 along the contour in Figures 1 and 2 and the angle $-\beta$ between the flat plate and the wake. Reflection of ζ, i.e. $\zeta \to -\zeta$, produces the opposite boundary of the analytically continued domain in the ζ-plane.

In actual practice w is eliminated between Eqs. (2-1) and (2-3) and the transformation of the blade and wake from z to ζ is obtained by complex Newton iteration proceeding from point to point around the contour. To ensure that the branch cuts of the two logarithms are never crossed, the arguments of these logs are monitored and if either one changes by more than $\pm\pi$ between adjacent points, the value of the associated log at the new point is incremented by $\mp 2\pi i$, i.e., in the opposite direction.

The final mapping transforms the infinite strip in the ζ-plane, bounded by the blade-wake contour and its reflection, into a rectangular domain with coordinates $F = \xi + i\eta$. If F is the complex potential for flow through the strip and we require $F(\zeta) = -F(-\zeta)$ and $\eta = -1$ along the contour, then F can be represented as a contour integral.

$$F(\zeta) = \frac{1}{2\pi i}\int_{-\infty}^{+\infty} \Phi(t) \log\frac{t+\zeta}{t-\zeta}\,dt + C\zeta \tag{2-4}$$

with $C = (2/h)\exp(-i\beta)$. Here C, β, and h are, respectively, the complex velocity, flow angle, and channel width in the far field. Now set

ORIGINAL PAGE IS
OF POOR QUALITY

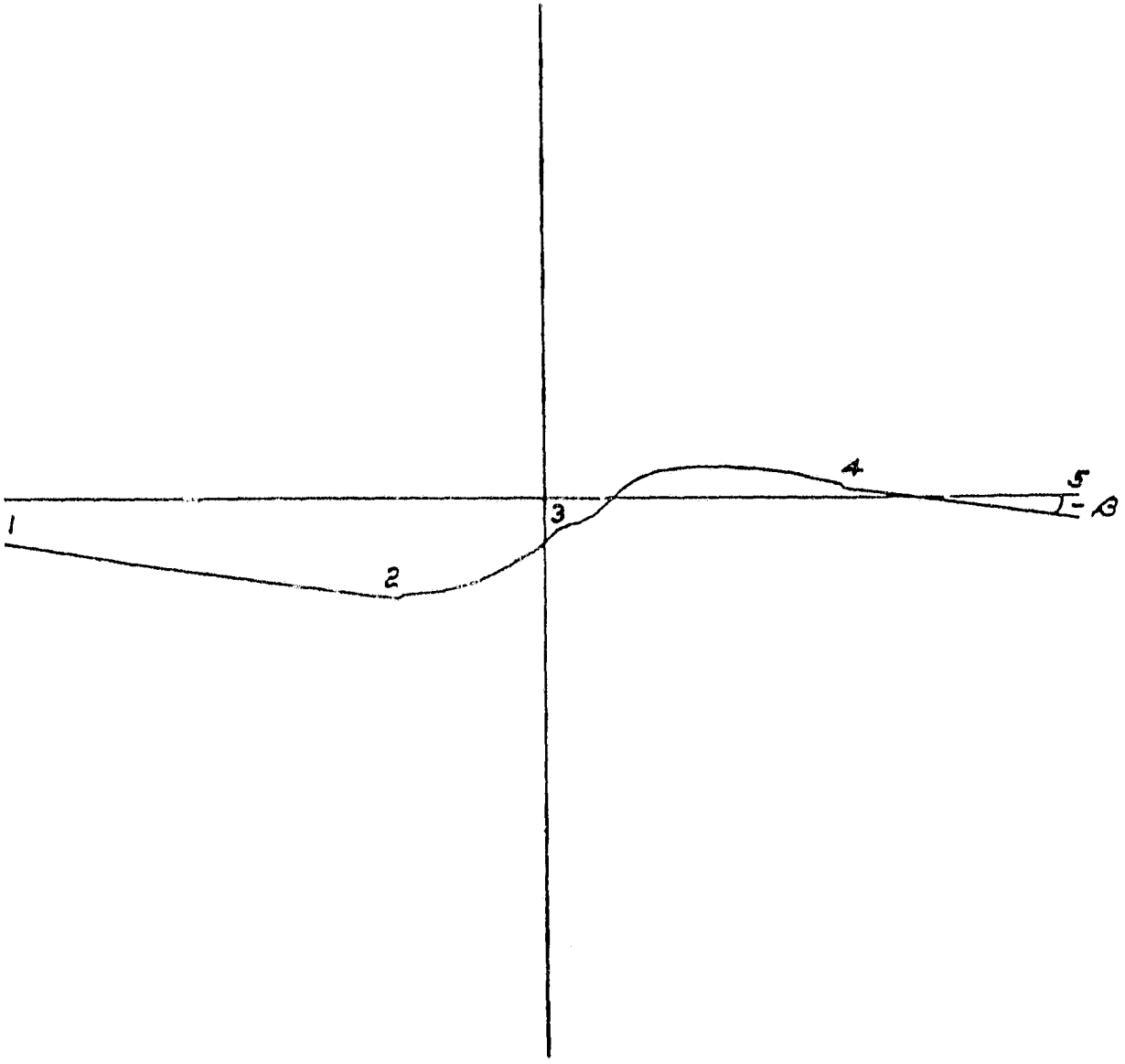

Figure 2. Image of Turbine Cascade and Wakes in ζ-Plane.

ORIGINAL PAGE IS
OF POOR QUALITY

$$\varphi \frac{dt}{ds} = q_t - i q_n \tag{2-5}$$

where s is arc length and q_t, q_n are the vortex and source densities, respectively. We choose q_n to cancel the normal component of C.

$$q_n = \mathrm{Im}\left(C \frac{dt}{ds}\right) \tag{2-6}$$

This should minimize the magnitude of q_t. For ζ on the contour, $\eta = -1$ and the imaginary part of eq. (2-4) gives an integral equation for q_t.

$$\frac{1}{2\pi} \int_{-\infty}^{\infty} \left[q_t \, \mathrm{Re}\left(\log \frac{t+\zeta}{t-\zeta}\right) + q_n \, \mathrm{Im}\left(\log \frac{t+\zeta}{t-\zeta}\right)\right] ds = 1 + \mathrm{Im}(C\zeta) \tag{2-7}$$

Equation (2-7) is solved by a simple panel method with flat panels and locally constant q_t and q_n. Once q_t is known, the real part of Eq. (2-4) gives ξ along the contour.

$$\xi = \mathrm{Re}(C\zeta) - \frac{1}{2\pi} \int_{-\infty}^{\infty} \left[q_n \, \mathrm{Re}\left(\log \frac{t+\zeta}{t-\zeta}\right) - q_t \, \mathrm{Im}\left(\log \frac{t+\zeta}{t-\zeta}\right)\right] ds \tag{2-8}$$

Generation of the grid in the rectangular (ξ,η) space proceeds in two stages. First, points are located on the boundaries such that the physical z-plane coordinates willbe periodic and continuous across the wake. As we shall see the $\eta = 0$ line transforms into the periodic boundary in the z-plane. Grid periodicity is enforced by distributing pairs of points symmetrically about the origin along the ξ-axis. Continuity across the far wake is achieved by selecting a constant mesh spacing in this region such that the z-plane spacing is an integer fraction of $(s)\sin|\beta_w|$ where β_w is

ORIGINAL PAGE IS
OF POOR QUALITY

the wake angle. Together these requirements imply that grid point location in (ξ,η) is an odd function of ξ which becomes linear for large $|\xi|$. A fifth order polynomial is used for small $|\xi|$ in order to provide for clustering around the leading edge. The values of ζ along the contour are found by inverse interpolation in the ξ vs ζ solution. In general the z-plane coordinates will still be discontinuous across the wake near the trailing edge as a result of contour curvature. A local straining is introduced to place a pair of points at the trailing edge and then pairs of neighboring points across the wake are adjusted until their z-plane images coincide. The distribution of points with η at the two ends of the domain is arbitrary and a linear variation is used here.

The interior values of ζ are obtained from a finite difference solution of the complex Laplace equation

$$\frac{\partial^2 \zeta}{\partial \xi^2} + \frac{\partial^2 \zeta}{\partial \eta^2} = 0 \qquad (2\text{-}9)$$

$$-\xi_{MAX} < \xi < \xi_{MAX} \quad , \quad -1 < \eta \leq 0$$

Values of ζ are specified along $\eta = -1$ and $\xi = \pm \xi_{MAX}$ and the anti-symmetry property is used along $\eta = 0$. An ADI relaxation procedure is used to solve the finite difference equations with the η-inversion for fixed ξ performed simultaneously with that for $-\xi$. Estimates of the maximum and minimum eigenvalues of the ξ and η matrices [15] are used to obtain a near optimum sequence of acceleration parameters. Figure 3 shows the grid distribution in the ζ-plane for the turbine cascade of Figure 1. The upper plot boundary corresponds to $\eta = 0$ and maps into the upper and lower periodic lines in the cascade plane.

ORIGINAL PAGE IS
OF POOR QUALITY

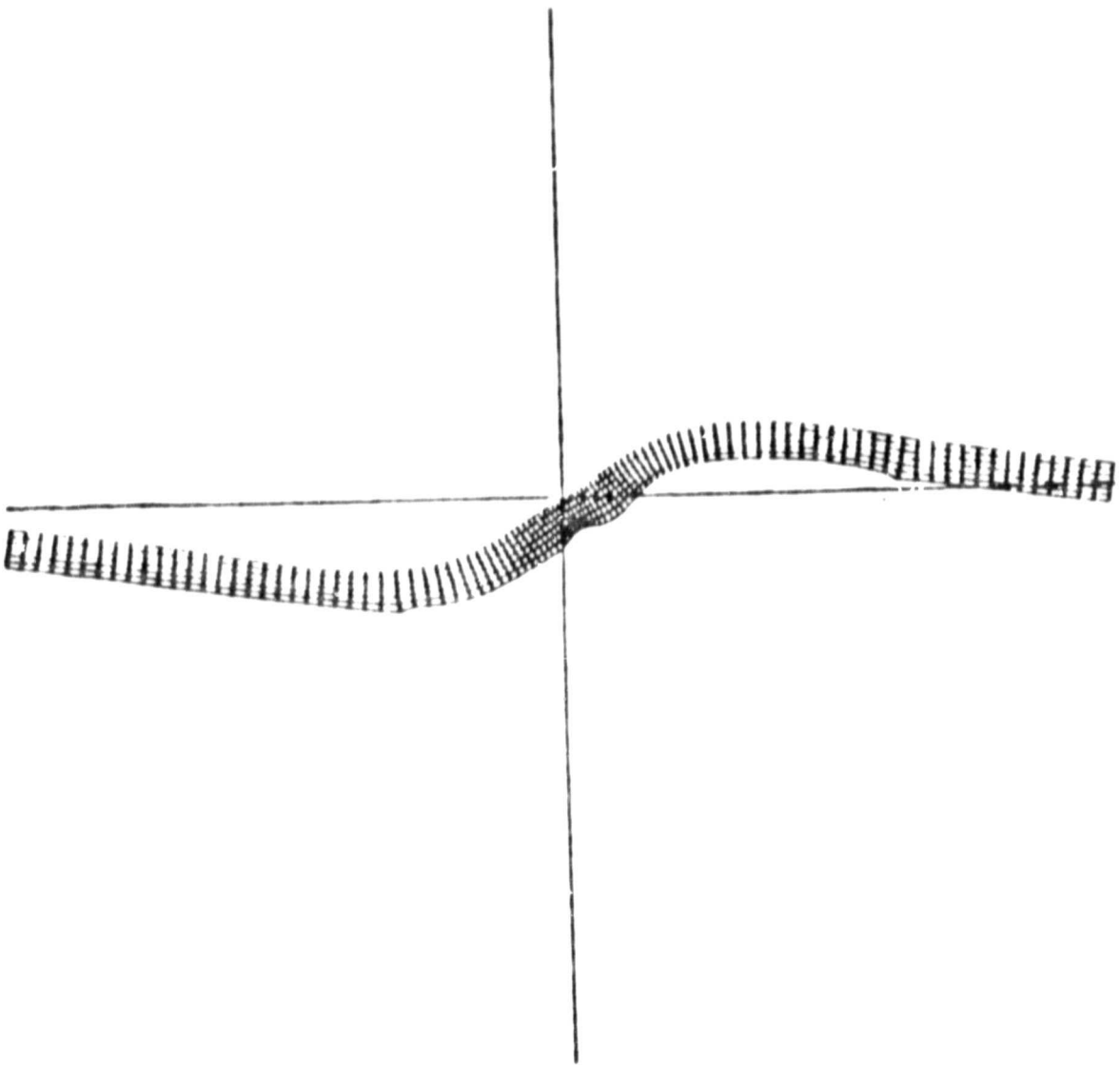

Figure 3. Turbine Cascade Grid in ζ-Plane.

ORIGINAL PAGE IS
OF POOR QUALITY

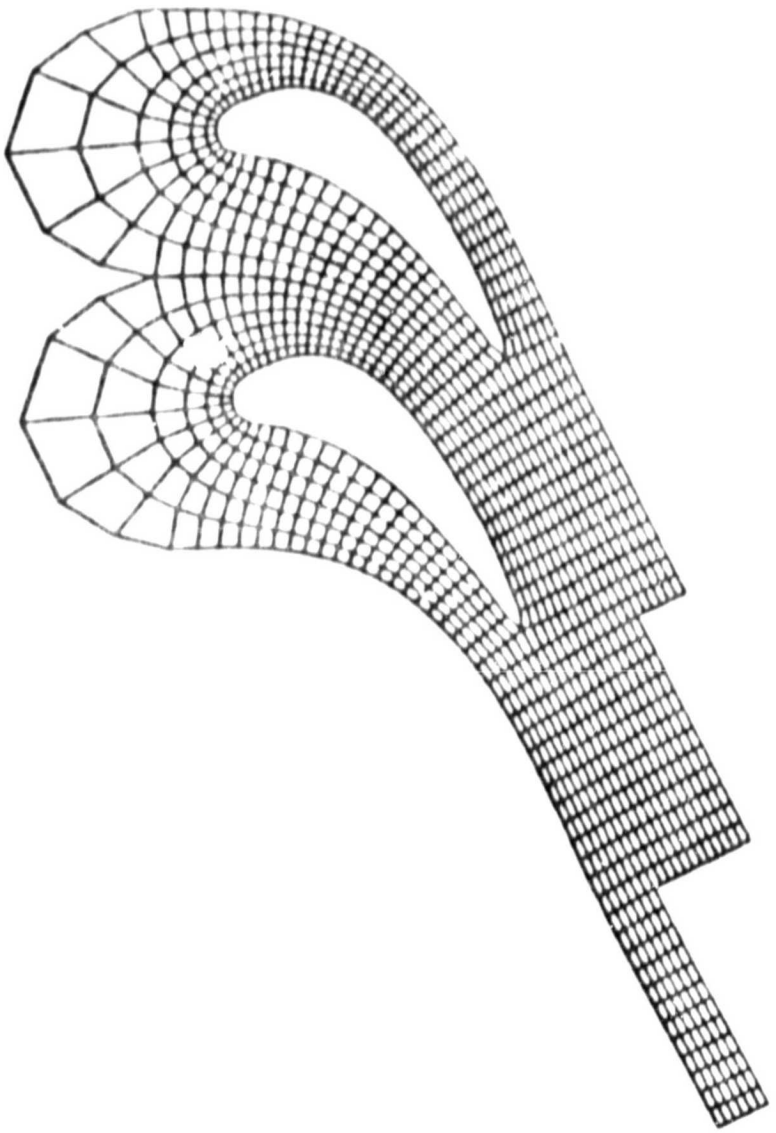

Figure 4. Turbine Cascade Grid in z-Plane.

The final grid in the z-plane (Figure 4) is obtained by conformal mapping from the ζ-plane using the two analytical functions (2-3) and (2-1). In this case continuity across the wake was obtained at the expense of a small amount of nonorthogonality. The rounded cap at the upstream boundary was obtained by extrapolation from the next two inner loops. Generation of this grid (99 x 7 points) required 1.4 seconds of CPU time on an IBM 3033 computer.

ORIGINAL PAGE IS
OF POOR QUALITY

III. THE INVISCID SOLUTION

The Euler equations are written in a conservative form appropriate for a general curvilinear coordinate system.

$$\frac{\partial Q}{\partial t} + \frac{\partial E}{\partial \xi} + \frac{\partial F}{\partial \eta} = 0 \tag{3-1}$$

where

$$Q = \frac{1}{J}\begin{bmatrix} \rho \\ \rho u \\ \rho v \\ e \end{bmatrix}, \quad E = \frac{1}{J}\begin{bmatrix} \rho U \\ \rho u U + \xi_x p \\ \rho v U + \xi_y p \\ (e+p)U \end{bmatrix}, \quad F = \frac{1}{J}\begin{bmatrix} \rho V \\ \rho u V + \eta_x p \\ \rho v V + \eta_y p \\ (e+p)V \end{bmatrix}$$

and where,

$$J = \xi_x \eta_y - \xi_y \eta_x$$
$$U = u\,\xi_x + v\,\xi_y$$
$$V = u\,\eta_x + v\,\eta_y$$

In this equation, u and v are the x and y components of velocity, while U and V represent the contravariant velocity components in the ξ and η directions. These directions and velocity components are shown in Figure 5 along with u_s and u_n, the physical velocity components that are respectively tangent and normal to an η= const. grid line. Also, ρ is the density, p is the pressure, e is the total energy per unit volume, and the fluid is assumed to obey the Perfect Gas Law. This equation was used by Steger in the study described in Reference [8], and since much of the theory of the inviscid solution used here is taken from that work, we will be content to present only a brief outline of this theory.

The solution of equation (3-1) is accomplished by an implicit time marching algorithm, which is expressed in the "delta form" (see [4]) as,

ORIGINAL PAGE IS
OF POOR QUALITY

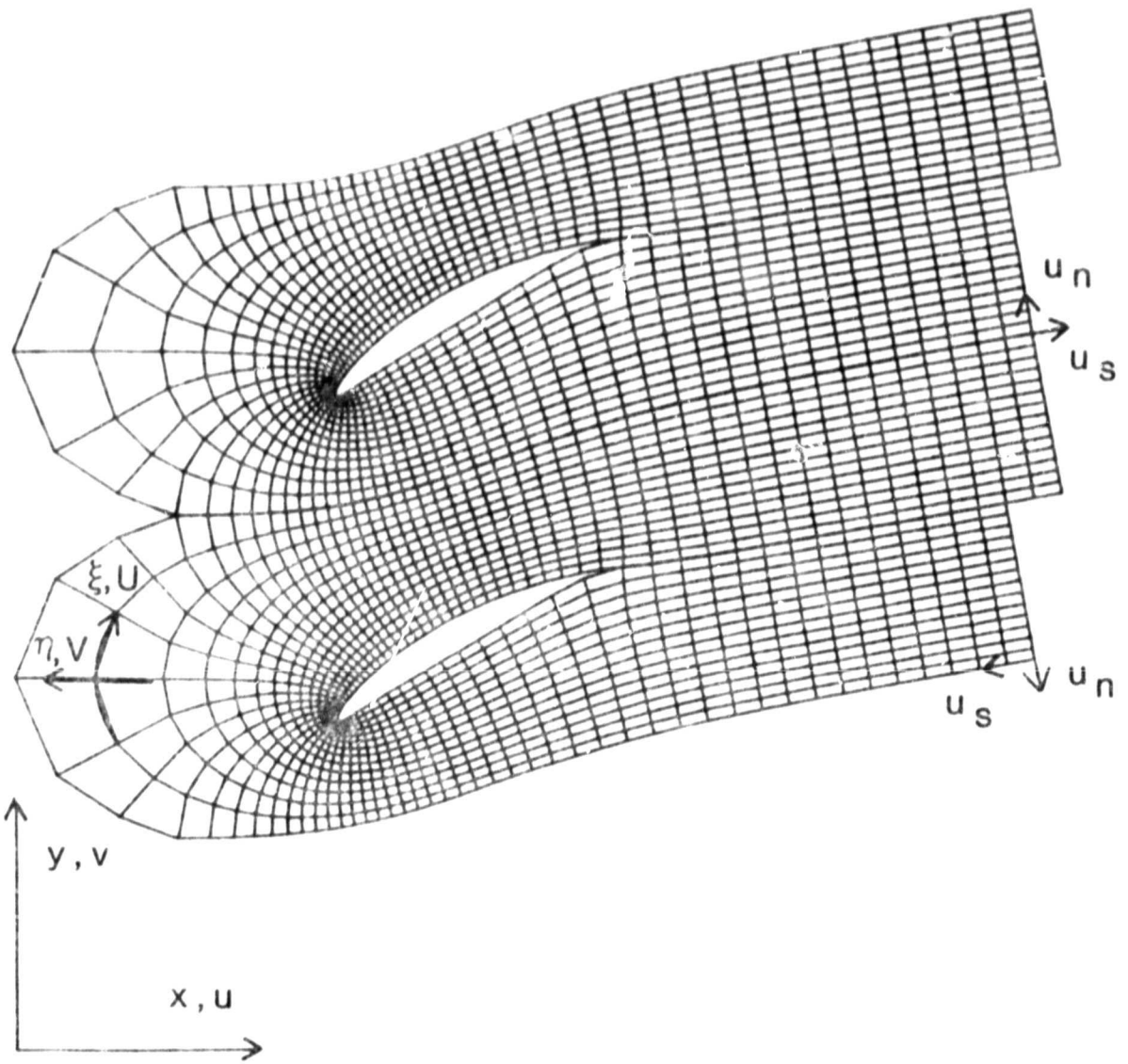

Figure 5. The cascade coordinate system.

ORIGINAL PAGE IS
OF POOR QUALITY

$$\left(I+\Delta t\frac{\partial}{\partial\xi}A^n-\frac{\epsilon_i}{J}\Delta\xi^2\frac{\partial^2}{\partial\xi^2}J\right)\left(I+\Delta t\frac{\partial}{\partial\eta}B^n\right.$$
$$\left.-\frac{\epsilon_i}{J}\Delta\eta^2\frac{\partial^2}{\partial\eta^2}J\right)\left(Q^{n+1}-Q^n\right)=-\Delta t\left(\frac{\partial E}{\partial\xi}^n+\frac{\partial F}{\partial\eta}^n\right)$$
$$-\frac{\epsilon_e}{J}\left(\Delta\xi^4\frac{\partial^4}{\partial\xi^4}J+\Delta\eta^4\frac{\partial^4}{\partial\eta^4}J\right)Q^n \qquad (3\text{-}2)$$

Here, A and B represent the Jacobian matrices $\left(\frac{\partial E}{\partial Q}\right)$ and $\left(\frac{\partial F}{\partial Q}\right)$, and the superscripts (n) and (n + 1) indicate the time level at which a quantity is evaluated. ϵ_i and ϵ_e are the coefficients for the artificial dissipation terms, which have been added to the algorithm in both an implicit and explicit manner as suggested in [16].

Boundary Conditions

For the description of the boundary conditions on the invisicid solution which follows, the reader may refer to Figure 5 where a typical computational grid mesh is displayed. Blade surface boundary conditions are obtained by first extrapolating ρ and U to the blade surface from the interior of the solution region. At the trailing edge, which is taken to be a cusp, extrapolated values of ρ, p, and $|U|$, are then averaged. The impermeability of the blade surface gives V = 0. Then the surface pressure is obtained by solving the tridiagonal system of equations that results from differencing the normal momentum equation

$$-\rho U(n_x u_\xi+n_y v_\xi)-\rho V(n_x u_\eta+n_y v_\eta)$$
$$=(n_x\xi_x+\xi_y n_y)p_\xi+(n_x^2+n_y^2)p_\eta \qquad (3\text{-}3)$$

Boundary conditions along the wake centerline and periodic boundaries are obtained by averaging extrapolated values of ρ, ρu, ρv, and e, at

coincident or periodic pairs of points. Along the unmatched portion of the wake centerline boundary, the averaging of extrapolated values is carried out between the unmatched boundary points and the point on the bottom of the centerline which is farthest downstream. This portion of the boundary of the computational domain is associated with the step-like form of the downstream boundary, which is introduced in an attempt to relieve the skewing in the coordinate system that would otherwise occur in highly staggered cascades. It may be seen in Figure 5, and in the other computational grids displayed in this paper, that the coordinate skewing that results in these step-like grids is acceptably slight. The reduction in skewing is achieved at the expense of introducing this anomalous portion of the boundary; however, the treatment of this boundary segment did not prove to be a difficult problem since the calculation appeared to be relatively insensitve to the boundary conditions applied at this location.

The treatment of the downstream boundary used here, follows the approach of Rudy and Strikwerda [17]. Their suggestion, for a rectangular computational domain with the downstream boundary oriented so that the outward normal is in the x-direction, was as follows. First, values of u, v, and T (temperature), are extrapolated to the boundary, and then the pressure is obtained by solving the equation,

$$\frac{\partial p}{\partial t} - \rho c \frac{\partial u}{\partial t} + \alpha (p - p_\infty) = 0 \qquad (3\text{-}4)$$

where:

c - local speed of sound

p_∞ - exit pressure of the converged solution

ORIGINAL PAGE IS
OF POOR QUALITY

α - a parameter whose value is chosen to optimize convergence

By analogy, for the more complicated domain of Figure 5, we extrapolate values of u, v, and T, and obtain the pressure by solving,

$$\frac{\partial p}{\partial t} - \rho c\left(\frac{1}{\sqrt{1+(g')^2}}\left(\frac{\partial u}{\partial t} + g'\frac{\partial v}{\partial t}\right)\right) + \alpha(p - p_\infty) = 0 \qquad (3\text{-}5)$$

where,

$g' - \left(\frac{dy}{dx}\right)_{\eta = \text{const.}}$ or equivalently $\left[-\left(\frac{n_x}{n_y}\right)\right]$

It may be seen in Figure 5 that the downstream boundary consists of two distinct and separate pieces; the approach to obtaining boundary values is the same at both the upper and lower portions of the downstream boundary. The solution of equation (3-4) is relatively easy to implement, since the only storage of values from the preceding time step required is at boundary points.

At the upstream boundary, our approach is to specify v, $\left(\frac{p}{\rho^\gamma}\right)$, and $\left(u + \frac{2c}{\gamma-1}\right)$, where γ is the ratio of specific heats. A value for $\left(u - \frac{2c}{\gamma-1}\right)$ at each upstream boundary point is then obtained from

$$\left(\frac{\partial}{\partial t} + (u-c)\frac{\partial}{\partial x}\right)\left(u - \frac{2c}{\gamma-1}\right) = 0 \qquad (3\text{-}8)$$

To solve equation (3-8), it is first rewritten as,

$$\left(\frac{\partial}{\partial t} + (u-c)\left(\xi_x\frac{\partial}{\partial \xi} + n_x\frac{\partial}{\partial n}\right)\right)\left(u - \frac{2c}{\gamma-1}\right) = 0 \qquad (3\text{-}9)$$

and then explicitly differenced in time. This simplified characteristics treatment of the upstream boundary is open to several objections, most notably perhaps in that the compatibility equation used here (equation (3-8)) is suitable for signal propagation in the negative x-direction.

However, signal propagation in a direction that is essentially normal to the boundary is what one usually tries to accomodate with the method of characteristics treatment of boundaries (see for example [18]), and it is easily seen in Figure 5 that the x-direction is at best only somewhat normal to the upstream boundary. While a more sophisticated treatment of the upstream boundary would be more esthetically pleasing, we have chosen the present approach because it does not appear to degrade the numerical solution in any way and it is comparatively easy to implement.

It is important to note that the boundary procedures described in this section were employed only after simpler approaches had failed. For example, the Rudy and Stridwerda approach to the downstream boundary was adopted after the method of extrapolating u, v, and T, and specifying p was found to cause the solution to become unstable. While such procedures are often employed in isolated airfoil calculations to assist with the convergence rate of the solution, it was our experience that in the absence of such precautions the cascade solution either converged to a result with noticeable errors or did not converge at all. It would appear that sophisticated boundary procedures, which can be an assistance for isolated airfoil calculations, are a necessity for cascades. In this regard we would mention specifically the nonreflecting downstream boundary condition, the characteristics treatment of the inflow boundary, and the use of the normal momentum equation to obtain the blade surface pressure.

IV. THE VISCOUS SOLUTION AND INTERACTIVE PROCEDURE

The viscous solution consists of a finite difference marching calculation which is capable of dealing with blade boundary layers on both the pressure and suction surfaces, and of proceeding from there directly into the blade wake. The calculation can accomodate a flow which is compressible and turbulent; the turbulence modeling used is the two layer algebraic eddy viscosity of Cebeci and Smith [19]. Additional features of the viscous solution include transition modeling [20], and a specialized turbulence modeling in the wake region [21]. The viscous calculation is initiated at the stagnation point in the following manner. First, the sign change of the velocity component u_s is used to determine the two adjacent blade surface points in the cascade grid which bracket the stagnation point*. Second, the values of u_s at these points are used to locate the stagnation point within the interval by interpolation, and the boundary layer is advanced to the bracket points by the similarity solution for stagnation point flow (see for example [22]). The suction surface and pressure surface calculations are then started from these locations and values. For the numerical marching calculation, we have employed a marching algorithm described in Reference [23].

*Since the contravariant velocity component U might seem to be the most obvious quantity to monitor for a sign change to locate the stagnation point, it is noted in passing that u_s and U do not necessarily share the same sign at blade surface points if there is a non-zero velocity component normal to the surface. A surface injection distribution is specified for subsequent inviscid solutions within the viscous-inviscid iterative process, so a non-zero normal velocity component can be expected in this calcuation. In this case, u_s and not U is the appropriate choice.

OF POOR QUALITY

Governing Equations

For the viscous marching calculation we take as the governing equations;

$$\frac{\partial}{\partial x}(\rho u) + \frac{\partial}{\partial y}(\overline{\rho v}) = 0 \tag{4-1}$$

$$\rho u \frac{\partial u}{\partial x} + (\overline{\rho v})\frac{\partial u}{\partial y} = \rho_\infty u_\infty \frac{\partial u_\infty}{\partial x} + \frac{\partial}{\partial y}\left(\mu \frac{\partial u}{\partial y} - \rho(\overline{u'v'})\right) \tag{4-2}$$

$$\rho u \frac{\partial h}{\partial x} + (\overline{\rho v})\frac{\partial h}{\partial y} = u\left(\rho_\infty \frac{\partial h_\infty}{\partial x}\right) + \frac{\partial}{\partial y}\left(\frac{\mu}{Pr}\frac{\partial h}{\partial y} - \rho(\overline{h'v'})\right) + \left(\mu \frac{\partial u}{\partial y} - \rho(\overline{u'v'})\right)\frac{\partial u}{\partial y} \tag{4-3}$$

$$p = \rho R T \tag{4-4}$$

$$\mu = \mu_{REF}\left(T / T_{REF}\right)^{\omega} \tag{4-5}$$

$$h = c_p T \tag{4-6}$$

where Pr, c_p, and ω, are taken as constants, and the subscript ∞ denotes evaluation at the free stream. (In contrast to the notation used with the inviscid solution, x and y are now used to denote the streamwise and streamnormal directions.) Furthermore if we write,

$$-\rho(\overline{u'v'}) = \rho \epsilon_m \frac{\partial u}{\partial y} \tag{4-7}$$

ORIGINAL PAGE IS
OF POOR QUALITY

and,

$$-\rho(\overline{v'h'}) = \rho \epsilon_h \frac{\partial h}{\partial y} \tag{4-8}$$

and let $\epsilon_m^+ = \frac{\epsilon_m}{\nu}$, $\epsilon_h^+ = \frac{\epsilon_h}{\nu}$, and $Pr_t = \frac{\epsilon_m^+}{\epsilon_h^+}$, where Pr_t is a specified constant, then Equations (4-2) and (4-3) may be rewritten as;

$$\rho u \frac{\partial u}{\partial x} + (\overline{\rho v}) \frac{\partial u}{\partial y} = \rho_\infty u_\infty \frac{\partial u_\infty}{\partial x} + \frac{\partial}{\partial y}\left(\mu(1+\epsilon_m^+)\frac{\partial u}{\partial y}\right) \tag{4-9}$$

$$\rho u \frac{\partial h}{\partial x} + (\overline{\rho v}) \frac{\partial h}{\partial y} = u\left(\rho_\infty \frac{\partial h_\infty}{\partial x}\right) + \mu(1+\epsilon_m^+)\left(\frac{\partial u}{\partial y}\right)^2 + \frac{\partial}{\partial y}\left(\frac{\mu}{Pr}\left(1+\epsilon_m^+ \frac{Pr}{Pr_t}\right)\frac{\partial h}{\partial y}\right) \tag{4-10}$$

Equations (4-1) and (4-4) - (4-10) form the basic system of equations which the marching calculation solves, exclusive of the turbulence modeling. To model the turbulence, the two-layer algebraic eddy viscosity of Cebeci and Smith [19] has been used.

For $y < y_1$, $\epsilon_m = \epsilon_{m_i}$

$$\epsilon_{m_i} = L^2 \left|\frac{\partial u}{\partial y}\right| \tag{4-11}$$

$$L = 0.4y(1 - \exp(-y/A)) \tag{4-12}$$

$$A = 26(\nu/u_\tau)\sqrt{\frac{\rho}{\rho_w}} \Big/ N \tag{4-13}$$

OF POOR QUALITY

$$N = \left(1 - 11.8\left(\frac{\mu_w}{\mu_\infty}\right)\left(\frac{\rho_\infty}{\rho_w}\right)^2 p^+\right)^{1/2} \tag{4-14}$$

$$p^+ = \left(\frac{\nu_\infty u_\infty}{u_\tau}\right)\frac{du_\infty}{dx} \tag{4-15}$$

$$u_\tau = \sqrt{\frac{\tau_w}{\rho_w}} \tag{4-16}$$

$$\tau_w = \left|\left(\mu \frac{\partial u}{\partial y}\right)_w\right| \tag{4-17}$$

where the subscript w indicates that a quantity is evaluated at the wall ($y = 0$).

For $y > y_1$, $\epsilon_m = \epsilon_{m_o}$

$$\epsilon_{m_o} = 0.0168\left|\int_0^\infty (u_\infty - u)\,dy\right| \tag{4-18}$$

The boundary between the inner and outer layers ($y = y_1$) is taken as the location where $\epsilon_{m_i} = \epsilon_{m_o}$.

Equations (4-11) - (4-18) are used to treat the blade boundary layers. In the wake the modeling used is somewhat different, and follows the three-layer approach described in Reference [21].

For $y < y_2$, $\epsilon_m = \epsilon_{m_s}$

$$\epsilon_{m_s} = 0.4\left(u_\tau\right)_{T.E.} Y_c \tag{4-19}$$

ORIGINAL PAGE IS
OF POOR QUALITY

where $y = y_c$ when $u = 1.10\ (u)_{T.E.}$, and the subscript T.E. denotes evaluation at the trailing edge.

For $y_2 < y < y_1$, $\epsilon_m = \epsilon_{m_i}$

Equation (4-11) is applied in this region with,

$$L = 0.4\,y \tag{4-20}$$

For $y > y_1$, $\epsilon_m = \epsilon_{m_o}$

Equation (4-18) is applied in this region without alteration.

The boundaries between the layers, $y = y_1$ and $y = y_2$, are taken as the locations where $\epsilon_{m_i} = \epsilon_{m_o}$ and $\epsilon_{m_s} = \epsilon_{m_i}$, respectively. Furthermore, if $\epsilon_{m_s} > \epsilon_{m_o}$, then ϵ_m is taken to equal ϵ_{m_o} for all y.

An additional feature of the turbulence modeling used in this study is the transition intermittency factor (γ_{tr}). This γ_{tr}, which multiplies the eddy viscosity determined from the preceding formulas, is calculated according to Equations (4-21) and (4-22) which follow from the work of Chen and Thyson [20].

$$\gamma_{tr} = 1 - \exp\left(-G \int_{x_{tr}}^{x} \frac{(x - x_{tr})}{u_\infty}\, dx\right) \tag{4-21}$$

$$G = .0008\left(\frac{u_\infty^3}{\nu_\infty^2}\right) Re_{x_{tr}}^{-1.34} \tag{4-22}$$

A value for the transition Reynolds number ($Re_{x_{tr}}$) is specified for the calculation.

ORIGINAL PAGE IS
OF POOR QUALITY

Grid Mesh for the Marching Calculation

The viscous marching calculation is carried out on a grid that is considerably more dense than the one used for the inviscid solution. In the streamwise direction along the blade surface and wake centerline, 30 boundary layer grid divisions correspond to each single inviscid solution grid space. In the direction normal to the blade and wake, a variable grid spacing technique described in Reference [19] has been employed in an attempt to better resolve the large gradients which characterize a turbulent shear layer. For this approach, in which the ratio (K) of consecutive grid spacings is fixed (i.e., $\frac{(\Delta y)_{j+1}}{(\Delta y)_j} = K$), values for the first grid interval $(\Delta y)_1$ and the ratio (K) are specified.

The Numerical Scheme

As mentioned previously, a marching algorithm described in [23] has been used in the viscous solution. For the grid system described in the preceding section, Equations (4-1), (4-9), and (4-10) result in the following finite difference equations.

$$\frac{\rho_{i+1,j+1}u_{i+1,j+1} - \rho_{i,j+1}u_{i,j+1}}{(\Delta x)_{i+1}} - \frac{(\overline{\rho v})_{i+1,j+1} - (\overline{\rho v})_{i+1,j}}{(\Delta y)_{j+1}} = 0 \qquad (4\text{-}23)$$

$$\rho_{i,j}u_{i,j}\frac{u_{i+1,j}-u_{i,j}}{(\Delta x)_{i+1}} + (\overline{\rho v})_{i,j}\frac{u_{i+1,j+1}-u_{i+1,j-1}}{(\Delta y)_j(1+K)} = \rho_{i,j}u_{i,j}\frac{(u_\infty)_{i+1}-(u_\infty)_i}{(\Delta x)_{i+1}}$$
$$+ \mu_{i,j}(1+(\epsilon_m^+)_{i,j})\left(\frac{u_{i+1,j+1}-(1+K)u_{i+1,j}+Ku_{i+1,j-1}}{\left(\frac{K(1+K)}{2}\right)(\Delta y)_j^2}\right) +$$
$$\left(\frac{u_{i,j+1}-u_{i,j-1}}{(\Delta y)_j(1+K)}\right)\left(1+(\epsilon_m^+)_{i,j}\right)\left(\frac{u_{i+1,j+1}-u_{i+1,j-1}}{(\Delta y)_j(1+K)}\right) + \qquad (4\text{-}24)$$
$$\mu_{i,j}\left(\frac{(\epsilon_m^+)_{i,j+1}-(\epsilon_m^+)_{i,j-1}}{(\Delta y)_j(1+K)}\right)\left(\frac{u_{i+1,j+1}-u_{i+1,j-1}}{(\Delta y)_j(1+K)}\right)$$

ORIGINAL PAGE IS
OF POOR QUALITY

$$\rho_{i,j}u_{i,j}\frac{h_{i+1,j}-h_{i,j}}{(\Delta x)_{i+1}}+(\overline{\rho v})_{i,j}\frac{h_{i+1,j+1}-h_{i+1,j-1}}{(\Delta y)_j(1+K)}=$$

$$u_{i,j}\left((\rho_\infty)_i\frac{(h_\infty)_{i+1}-(h_\infty)_i}{(\Delta x)_{i+1}}\right)+\mu_{i,j}\left(1+(\epsilon_m^+)_{i,j}\right)\left(\frac{u_{i+1,j+1}-u_{i+1,j-1}}{(\Delta y)_j(1+K)}\right)^2$$

$$+\frac{\mu_{i,j}}{Pr}\left(1+(\epsilon_m^+)_{i,j}\frac{Pr}{Pr_t}\right)\left(\frac{h_{i+1,j+1}-(1+K)h_{i+1,j}+Kh_{i+1,j-1}}{(K(K+1)/2)(\Delta y)_j}\right)+$$

$$\frac{1}{Pr}\left(\frac{u_{i,j+1}-u_{i,j-1}}{(\Delta y)_j(1+K)}\right)\left(1+(\epsilon_m^+)_{i,j}\frac{Pr}{Pr_t}\right)\left(\frac{h_{i+1,j+1}-h_{i+1,j-1}}{(\Delta y)_j(1+K)}\right)+$$

$$\frac{\mu_{i,j}}{Pr_t}\left(\frac{(\epsilon_m^+)_{i,j+1}-(\epsilon_m^+)_{i,j-1}}{(\Delta y)_j(1+K)}\right)\left(\frac{h_{i+1,j+1}-h_{i+1,j-1}}{(\Delta y)_j(1+K)}\right) \qquad (4\text{-}25)$$

The system of difference equations consisting of (4-23), (4-24), and (4-25), together with the various property relations and turbulence equations, are solved subject to appropriate boundary conditions These boundary conditions are applied at free stream, blade surface, and wake centerline locations; it is in this regard that we mention the one-sided difference representation of $\frac{\partial h}{\partial y}$.

$$\left.\frac{\partial h}{\partial y}\right|_{i,j}=\frac{-h_{i,j+2}+4h_{i,j+1}-3h_{i,j}}{(3-K)(\Delta y)_{j+1}} \qquad (4\text{-}26)$$

The procedure for advancing the solution from the (i) station (presumed known to the (i+1) station (presumed unknown) is as follows:

(i) Solve Equation (4-24) to obtain $u_{i+1,j}$ for all j. A tridiagonal inversion is required.

(ii) Solve Equation (4-25) to obtain $h_{i+1,j}$ for all j. A tridiagonal inversion is required. (Due to the adiabatic wall and wake centerline symmetry boundary conditions, $\frac{\partial h}{\partial y}=0$ at y = 0, the matrix is not tridiagonal, but it will take this form after one Gaussian

elimination step. A similar preconditioning of the matrix is required when solving Equation (4-24) in the wake).

(iii) Equation (4-4) and (4-5) and (4-6) are solved for $T_{i+1,j}$, $\rho_{i+1,j}$, and $\mu_{i+1,j}$.

(iv) Equation (4-23) is marched from y = 0 to the outer edge of the shear layer to obtain $(\overline{\rho v})_{i+1,j}$.

(v) The turbulence modeling equations ((4-11)- (4-22)) are solved to obtain $(\epsilon_m^+)_{i+1,j}$.

The solution has now been advanced to station (i+1). Although this numerical scheme is a low order method, we have found it to be simple, inexpensive, and very stable. We have perceived these virtues of the method in a previous study [24], as well as in the present work. The reliability of the method was an important feature in a calculation that was expected to encounter laminar-turbulent transition, boundary layer separation, and the sudden change in boundary conditions that occurs when marching off the trailing edge and into the wake. It was for this reason that our first choice of a marching algorithm, the Keller Box Method (see for example [19]), which is significantly more accurate than the present scheme, was replaced with a method which appeared to be less sensitive. We have attempted to compensate for the lower accuracy of the method by an increase in grid density.

Additional Computational Features

Two additional computational features of the viscous solution remain to be discussed. As the first of these, it is noted that the calculation procedure includes provisions for extending the grid in the y-direction, should the shear layer approach the outer edge of the grid too closely. This feature enables the calculation region to grow with the boundary layer and to

contain it as economically as possible. Second, to equip this direct boundary layer solver with at least some ability to cope with regions of separated flow, we have altered the streamwise convection terms in Equations (4-24) and (4-25) for reverse flow in the manner of Rehyner and Flugge-Lotz [25].

The Interactive Procedure

The interactive procedure in this calculation consists of an iteration between the inviscid and viscous solutions previously described. The effect of the presence of the viscous shear layer on the inviscid solution, is modeled as a source-sink distribution along the blade surface and wake centerline. This source-sink distribution is obtained from the viscous solution according to the following expression;

$$\rho u_n = \frac{d}{dx} \int_0^\infty (\rho_\infty u_\infty - \rho u)\, dy \qquad (4\text{-}27)$$

where the notation used in the viscous solution (Section IV) appears on the right side of this equation, and the left side conforms to the notation of the inviscid solution (Section III). Once values of (ρu_n) have been calculated and supplied to the succeeding inviscid solution, there are some alterations in the treatment of the blade surface and wake centerline boundary conditions which we described Section III.

Blade surface boundary conditions retain the form described earlier, except that the specification of V = 0 is replaced with the specification of (ρu_n). The surface pressure is still obtained by a tridiagonal numerical solution of Equation (3-3). Along the wake centerline, values of (ρu_n) calculated from the preceding viscous solution are summed at coincident

points, and these sums are taken to represent a discontinuity in the values of $|\rho u_n|$ at those locations. The equality of ρ, u_s, and p, at coincident points is enforced by averaging extrapolates.

V. NUMERICAL RESULTS AND DISCUSSION

The results that have been obtained with the numerical procedure described in the preceding sections are presented here. The procedure has been applied to three cascades: an unstaggered cascade of NACA 0012 blades with a gap-chord ratio of (1.0), a 45° staggered cascade of NACA 65-410 blades with a gap-chord ratio of (0.777860), and a 28.5° staggered cascade of NACA 65-(12)10 blades with a gap-chord ratio of (1.0). Results are presented for several different flow situations in each of the three cascades including different Mach numbers and angles of attack. In certain cases where the viscous marching solution was incapable of dealing with the separated regions that occurred, and it was therefore impossible to perform an interactive calculation, we have presented results from the sole inviscid solution. The cascade of NACA 0012 blades and the cascade of NACA 65-410 blades were chosen as simple test cases to evaluate the performance of the numerical procedure. The cascade of NACA 65-(12)10 blades has been the subject of an experimental study of Briggs [26], and was chosen as it afforded the oportunity for comparison with experimental results. It is hereafter referred to as the Briggs cascade. The results obtained in each of the three cascades are discussed separately. However, the blade chord length is .25 ft and the flow is air in all of the test cases considered.

Unstaggered Cascade (NACA 0012 blades)

An unstaggered cascade of NACA 0012 blades with a gap-chord ratio of (1.0) was chosen for use in the initial tests of the numerical procedure, with the idea that an unstaggered cascade of symmetric airfoils would minimize the geometry related difficulties and would permit attention to be focused on other computational aspects of the method. The grid system used for this cascade is shown in Figure 6.

ORIGINAL PAGE IS
OF POOR QUALITY

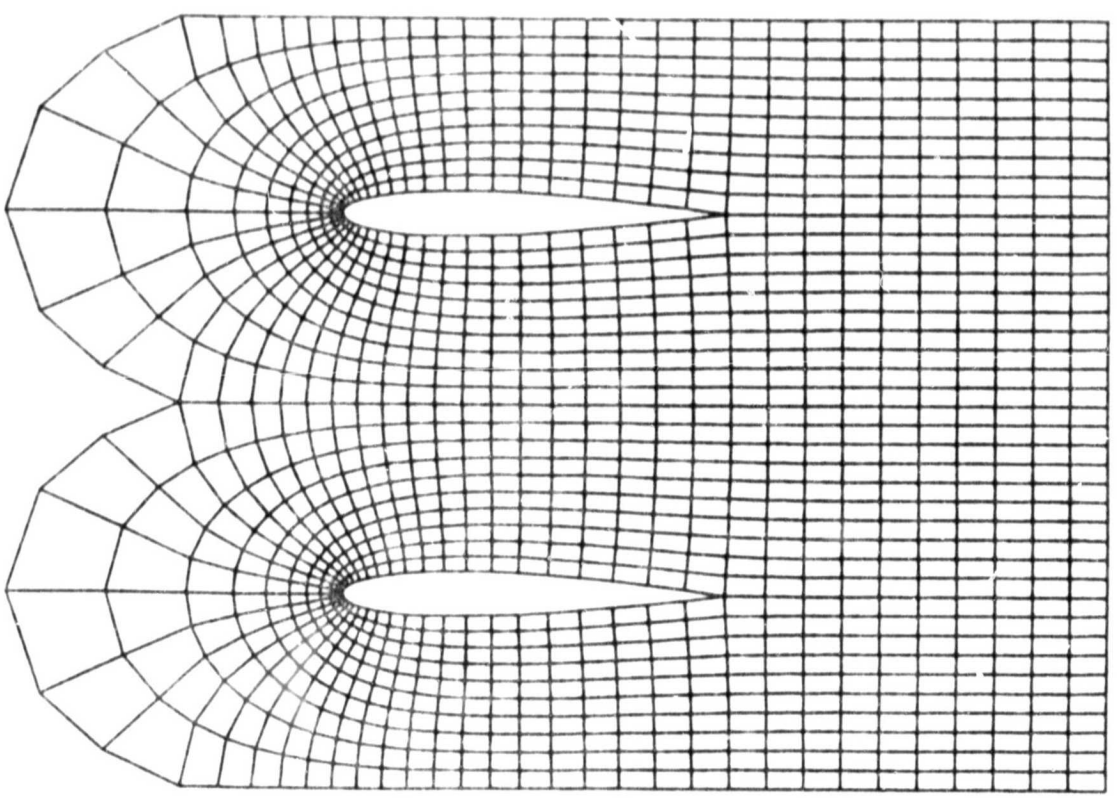

Figure 6. Grid system, unstaggered cascade (NACA 0012 blades).

ORIGINAL PAGE IS
OF POOR QUALITY

A subsonic flow at zero angle of attack was chosen as a first test case for the interactive calculation procedure. More precisely, for the upstream and downstream boundary conditions on the invscid solution we have specified the following:

Upstream Tangential Velocity ($v|_{x=-\infty}$) - 0.ft/sec

Upstream Riemann Invariant $\left(\left(u + \frac{2c}{\gamma-1}\right)\Big|_{x=-\infty}\right)$ - 5980. ft/sec

Upstream Isentropic Constant $\left(\left(p/\rho^{\gamma}\right)\Big|_{x=-\infty}\right)$ - 948210. (p - lbf/ft^2, ρ - slugs/ft^3)

Exit Pressure of the Converged Solution p_∞ - 2125. lbf/ft^2

The specifications result in a velocity of 496 ft/sec and a Mach number of (.45) at the upstream boundary.

The interactive calculation procedure was run for four global viscous-inviscid iterations in this test case with no apparent difficulty; a sampling of the results may be found in Figures 7-9. In Figure 7, values of the pressure coefficient on the blade surface $\left(C_p = \frac{p - p_\infty}{\frac{1}{2}\rho u^2|_{x=-\infty}}\right)$ from the first and last (fourth) inviscid solutions are displayed. Surface pressure coefficient values have been plotted for all grid points on the top and bottom surfaces of the blade; however, due to the symmetry in this flow situation, these values for corresponding points on the top and bottom are largely indistinguishable. This figure demonstrates the expected result that for the case under consideration, the fluid viscosity has only a slight influence on the surface pressure. In Figure 8, the convergence history of each of the four inviscid solutions is shown. The maximum residual, the decay of which is monitored in these plots, is calculated according to the expression $\left|\frac{\Delta p}{p_\infty}\right|_{MAX}$ where Δp is the change in

ORIGINAL PAGE IS
OF POOR QUALITY

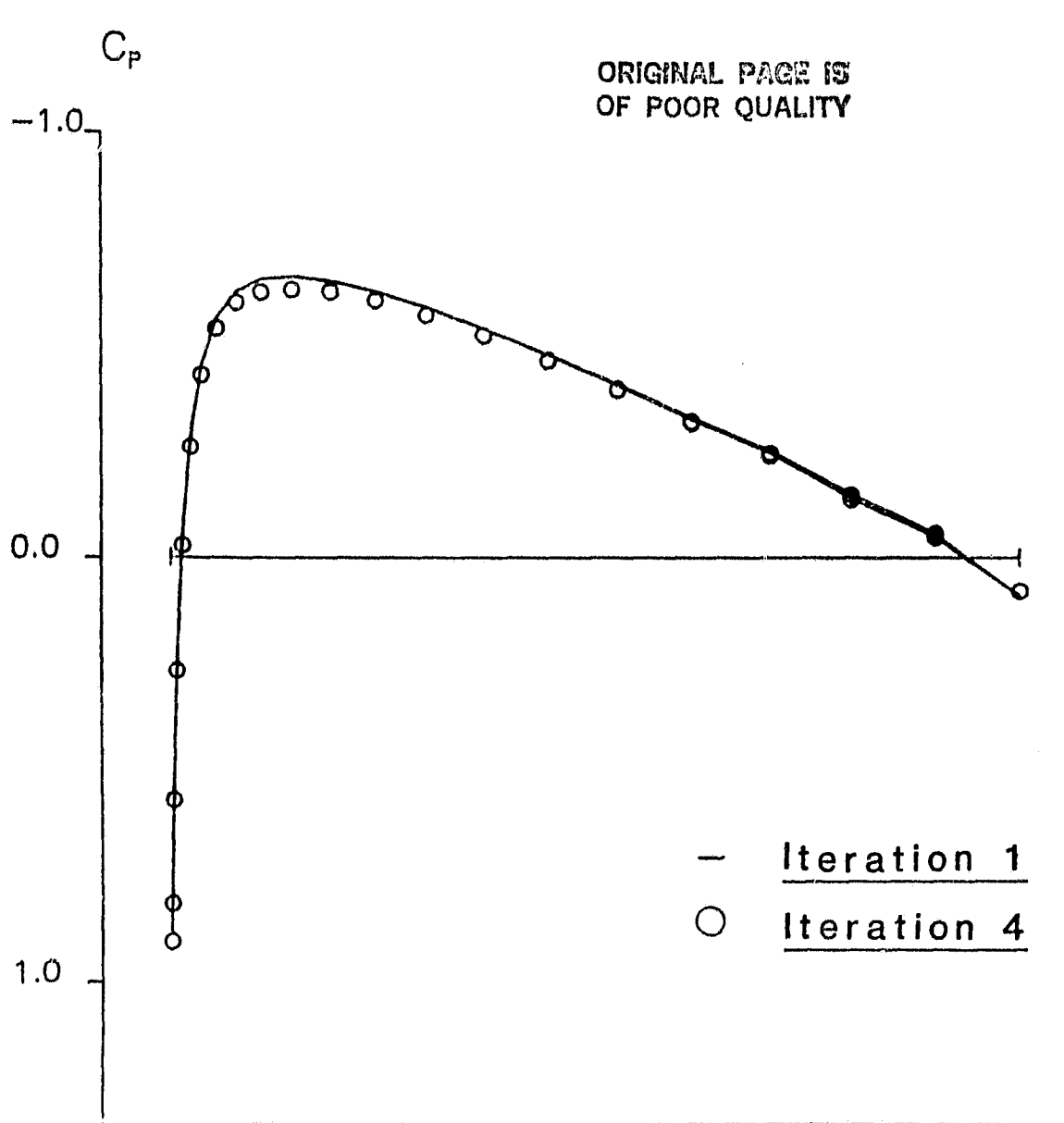

Figure 7. Surface pressure coefficient (NACA 0012 cascade, $M|_{X=-\infty}=.45$).

ORIGINAL PAGE IS
OF POOR QUALITY

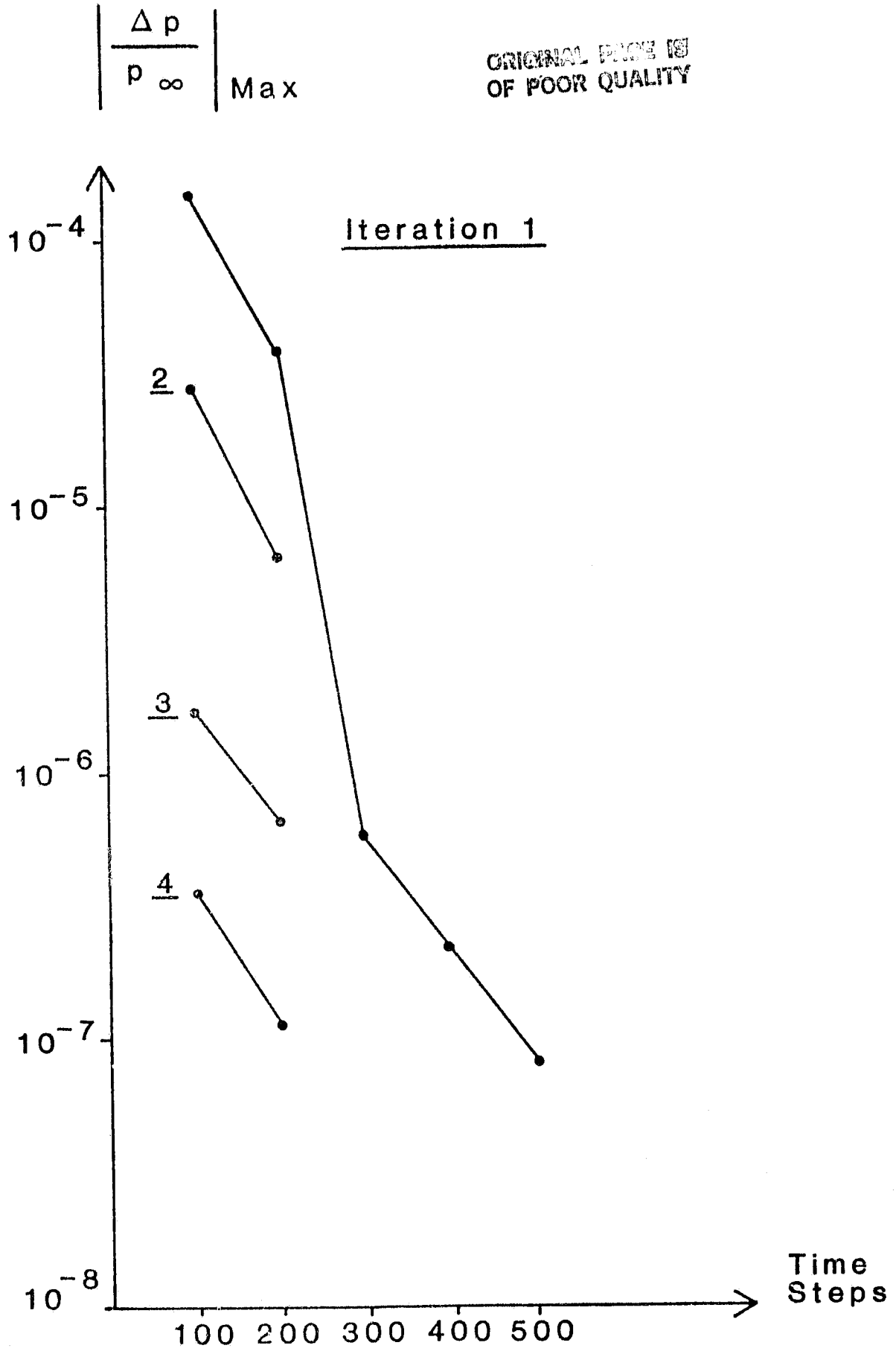

Figure 8. Maximum residual history.

ORIGINAL PAGE IS
OF POOR QUALITY

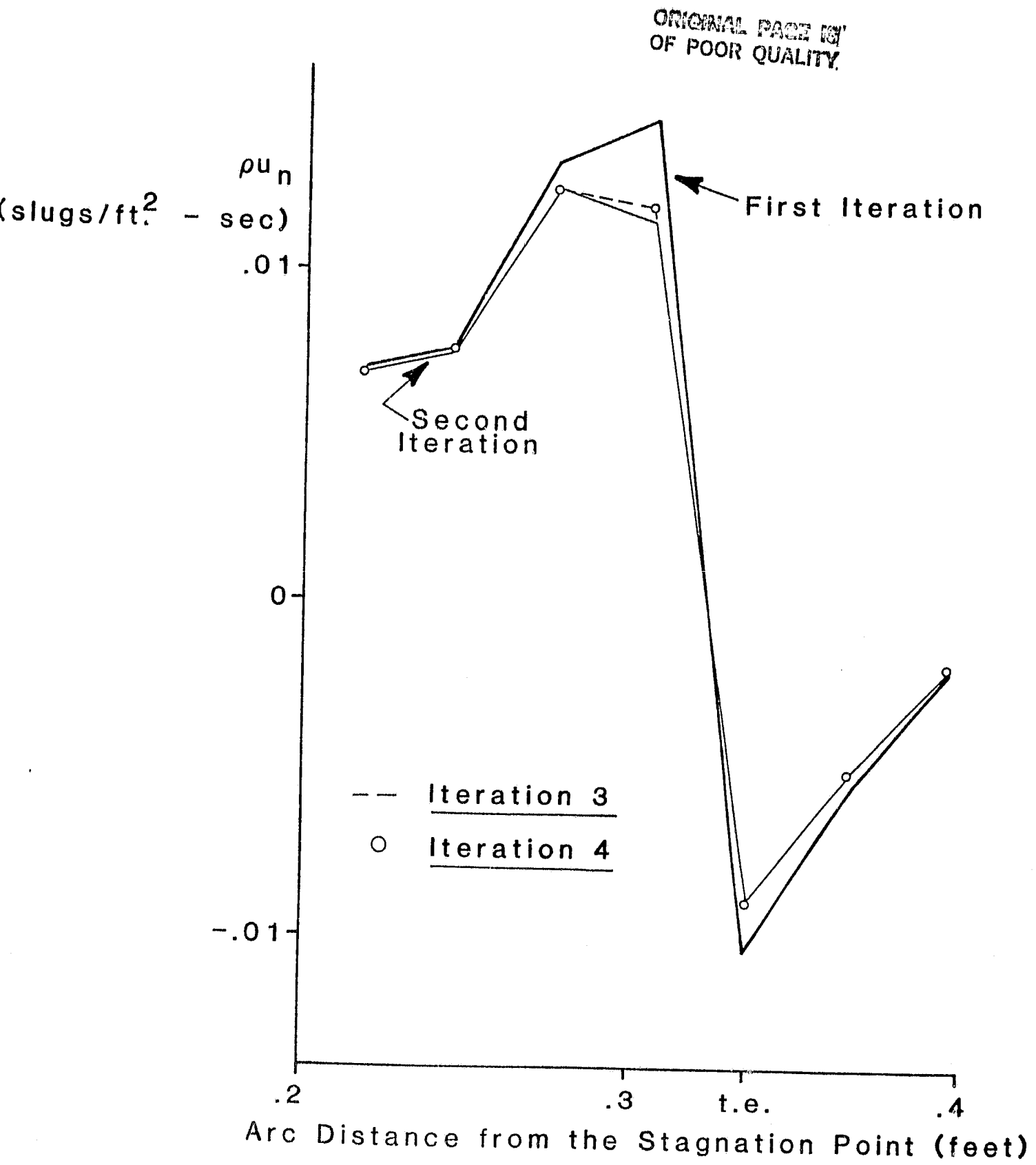

Figure 9. Mass injection rate.

pressure that occurs between two consecutive time steps, p_∞ is the exit presssure, and where points along the blade surface and wake centerline have been examined. The trend towards convergence, in both the time marching inviscid solutions and the global viscous-inviscid iteration, is apparent. Further evidence of the convergence of the method is shown in Figure 9, where plots showing the behavior of the mass injection rate (ρu_n) for each of the four global iterations are found. This behavior is examined in a region centered about the trailing edge (t.e.), as this region is one of special importance and sensitivity. Again, a trend towards convergence is indicated.

For this calculation, a time step was used which was estimated to be about 20 times larger than the Courant - Friederichs - Lewy (C.F.L.) Limit based on the smallest grid spacing in the field. This value was chosen as it was about the largest time step that could be used without destabilizing the calculation. The time step was held fixed throughout the calculation; no attempt was made to improve the convergence rate by cycling or varying the time step in any way, nor was it necessary to use a smaller initial time step to accomodate the calculation's impulsive start. (The only concession made to this impulsive start was to enforce the impermeability of the blade surface gradually, over 50 time steps.) The time step size did not differ greatly from this value in any of the test cases described in this section. For the artificial dissipation terms that appear in the inviscid solution algorithm, values of $\epsilon_e = .05$ and $(\epsilon_i/\epsilon_e) = 2$ were used in this test case, and similar values were used in all subsequent calculations. The value of 2 followed from suggestions made in Reference [16], while $\epsilon_e = .05$ was chosen as it was about the largest value which did

not destabilize the calculation. The numerical evidence of this and subseqent calculations was that a stability limit of approximately (.06) existed for ϵ_e. This observation conflicts with Reference [16], where the introduction of implicit damping (ϵ_i) is advocated as a means of relieving a stability limit on the basic algorithm (i.e. $\epsilon_i = 0$) of $\epsilon_e < \frac{1}{16}$ (= 0.625). This point will receive additional comment later in this section.

As a second test case for the the interactive calculation procedure, a flow into the unstaggered cascade at a 2^o angle of attack was considered, with a Mach number of (.45) at the upstream boundary. This flow situation was chosen as a simple test of the ability of the method to treat a lifting cascade. An interactive solution of three viscous-inviscid iterations was performed, the convergence history of which differed very little from the preceding test case. Values of the surface pressure coefficient from the first and last inviscid solutions are shown in Figure 10. Again, the fluid viscosity has an effect on the surface pressure distribution which though noticeable is small.

In the third and fourth test cases, situations have been considered where the effect of viscosity on the flow was more pronounced and the need for a viscous-inviscid interactive capability more clearly demonstrated. Both of these test cases involve flows in the unstaggered cascade at zero angle of attack, but higher Mach numbers. The third test case involved a subsonic flow with an upstream Mach number of (.63). The surface pressure coefficient for this case, which is shown in Figure 11, displays a larger difference between the first and last solutions in the iteration, than appeared in the previous test cases. The effect of the viscosity on the surface pressure is still more apparent if we consider a transonic flow

ORIGINAL PAGE IS
OF POOR QUALITY

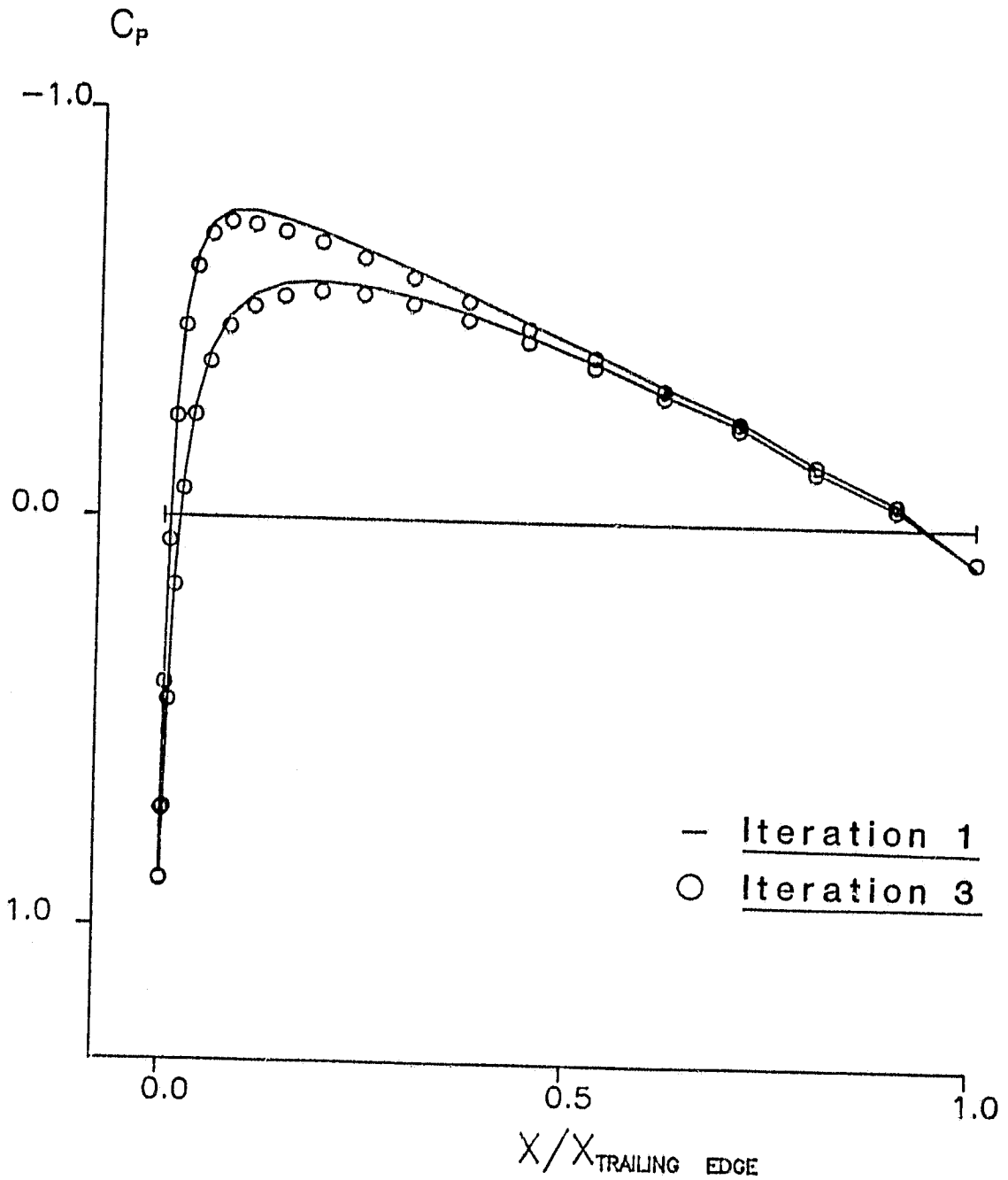

Figure 10. Surface pressure coefficient (NACA 0012 cascade, $M|_{x=-\infty} = .45$, 2° angle of attack).

ORIGINAL PAGE IS
OF POOR QUALITY

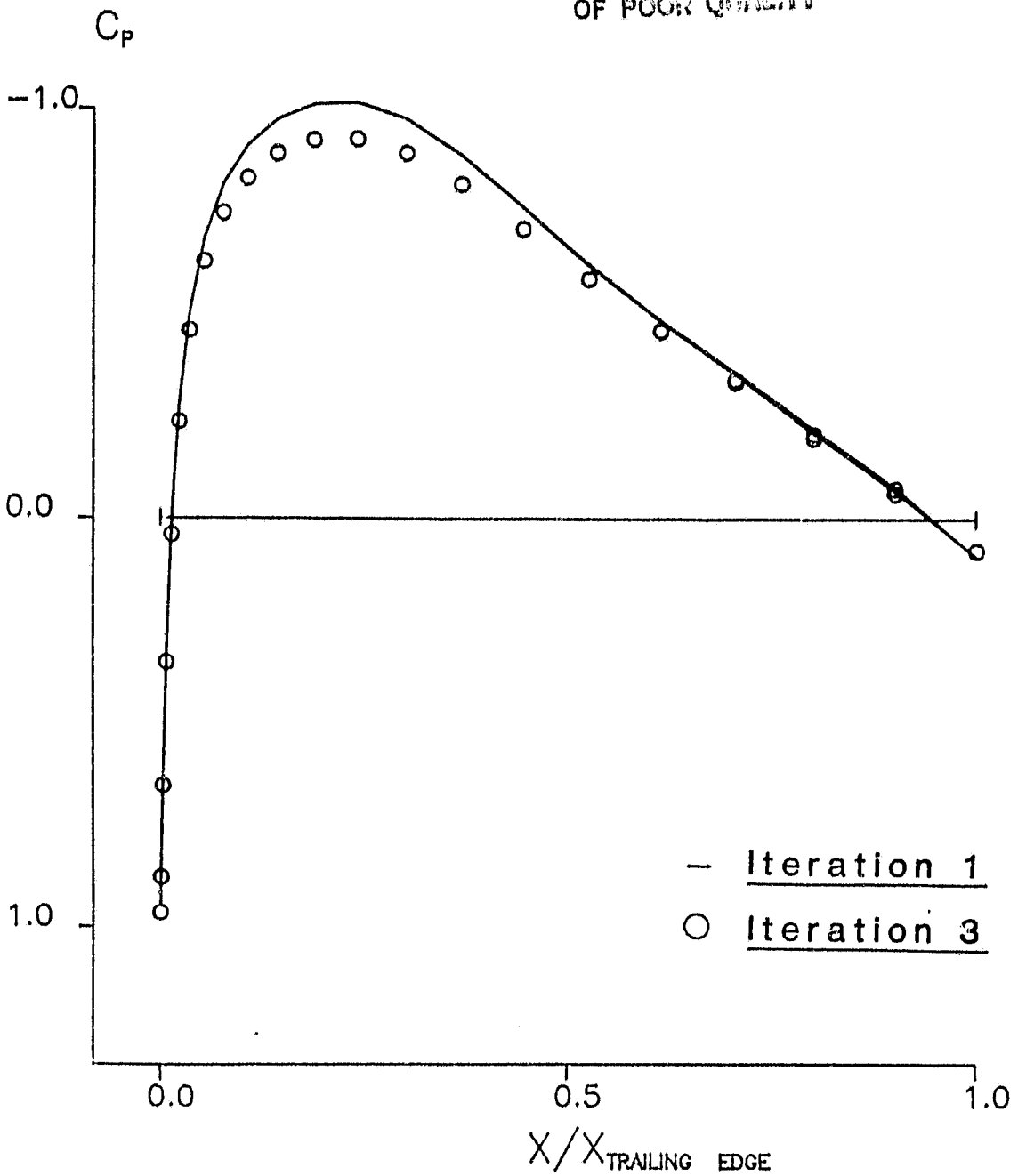

Figure 11. Surface pressure coefficient (NACA 0012 cascade, $M|_{X=-\infty}=.63$).

ORIGINAL PAGE IS
OF POOR QUALITY

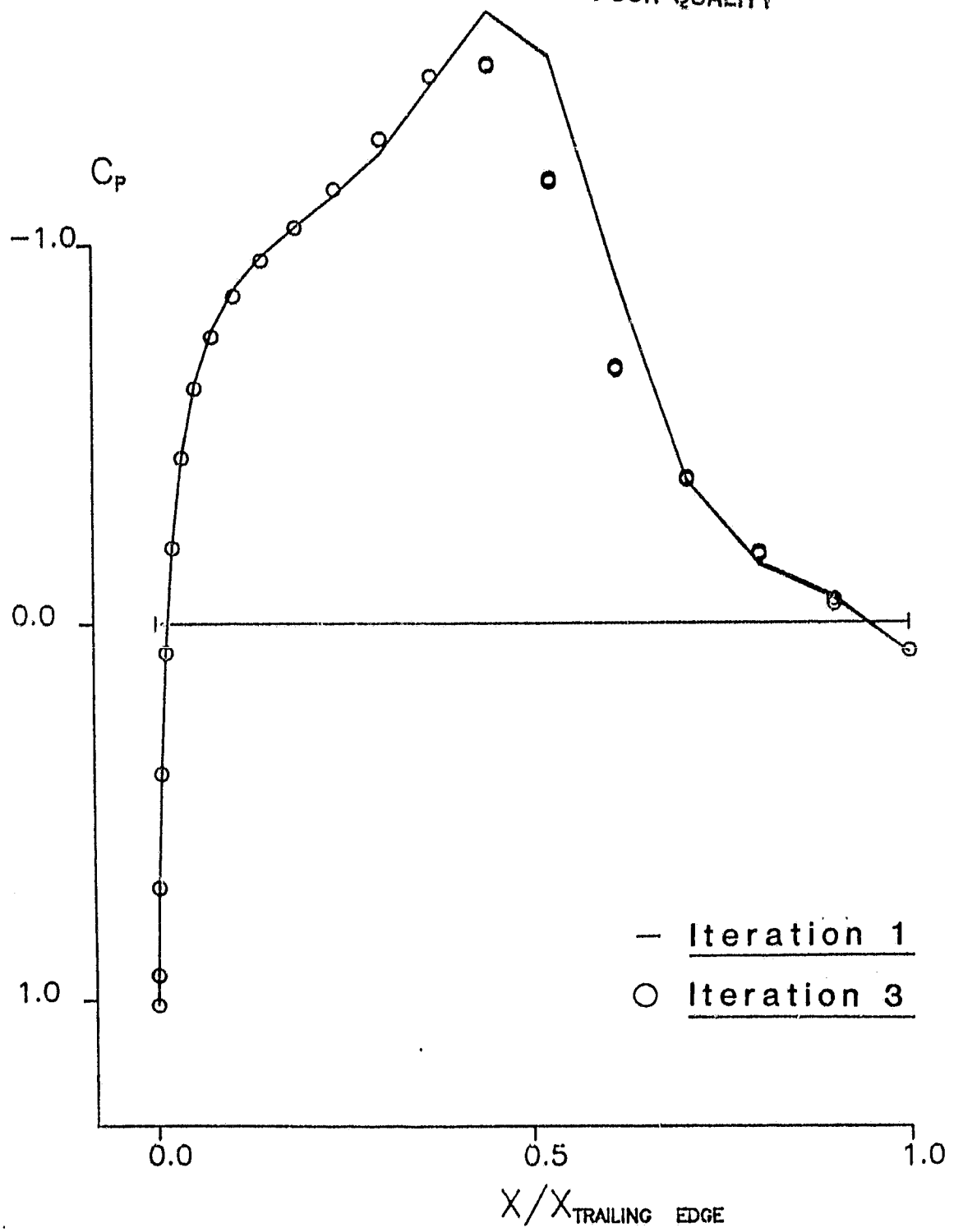

Figure 12. Surface pressure coefficient (NACA 0012 cascade, $M|_{X=-\infty}$=.65).

ORIGINAL PAGE IS
OF POOR QUALITY

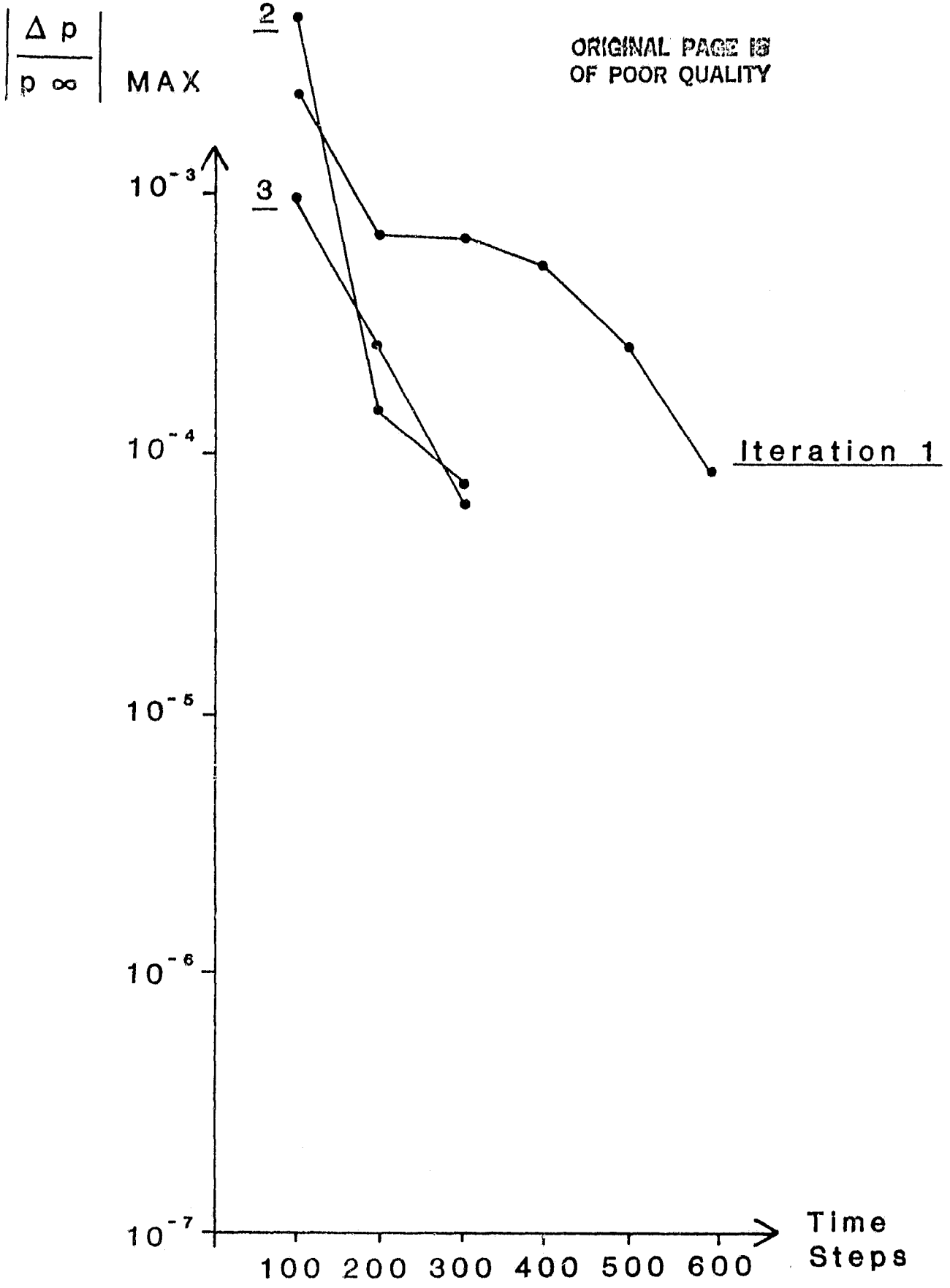

Figure 13. Maximum residual history.

situation such as the fourth test case, with an upstream Mach number of (.65). The surface pressure coefficient for this test case, shown in Figure 12, indicates that a shock is now present in the cascade. While the shock resolution in this case appears to be only fair, this shock smearing enables our direct boundary layer solver to negotiate the region of shock impingment on the boundary layer, and makes a viscous-inviscid iterative solution possible in this test case. We will return to the discussion of shock resolution and its implications for the viscous solution later in this section. For the present it will suffice to mention than the iterative solution converged successfully although not as quickly as in the subsonic test cases, and that the convergence history of this solution is found in Figure 13.

45° Staggered Cascade (NACA 65-410 blades)

A cascade of NACA 65-410 blades staggered at a 45° angle with a gap-chord ratio of (0.777860) was chosen to test the numerical procedure on a more geometrically difficult cascade. The grid system used for this cascade is shown in Figure 14. A subsonic flow that was well aligned with the blades was chosen for the first test case, with a Mach number of (.47), and a flow angle of 48.4° (i.e., an angle attack of 3.4°) at the upstream boundary. An interactive solution of three iterations was performed, the results of which are displayed in Figure 15. Also, the convergence history of this solution is shown in Figure 16.

An interesting feature of the surface pressure distribution in Figure 15 is the very low pressure that occurs on the pressure surface near the leading edge. In the second test case for this cascade, we sought to eliminate this feature by increasing the flow angle at the entrance. The

ORIGINAL PAGE IS
OF POOR QUALITY

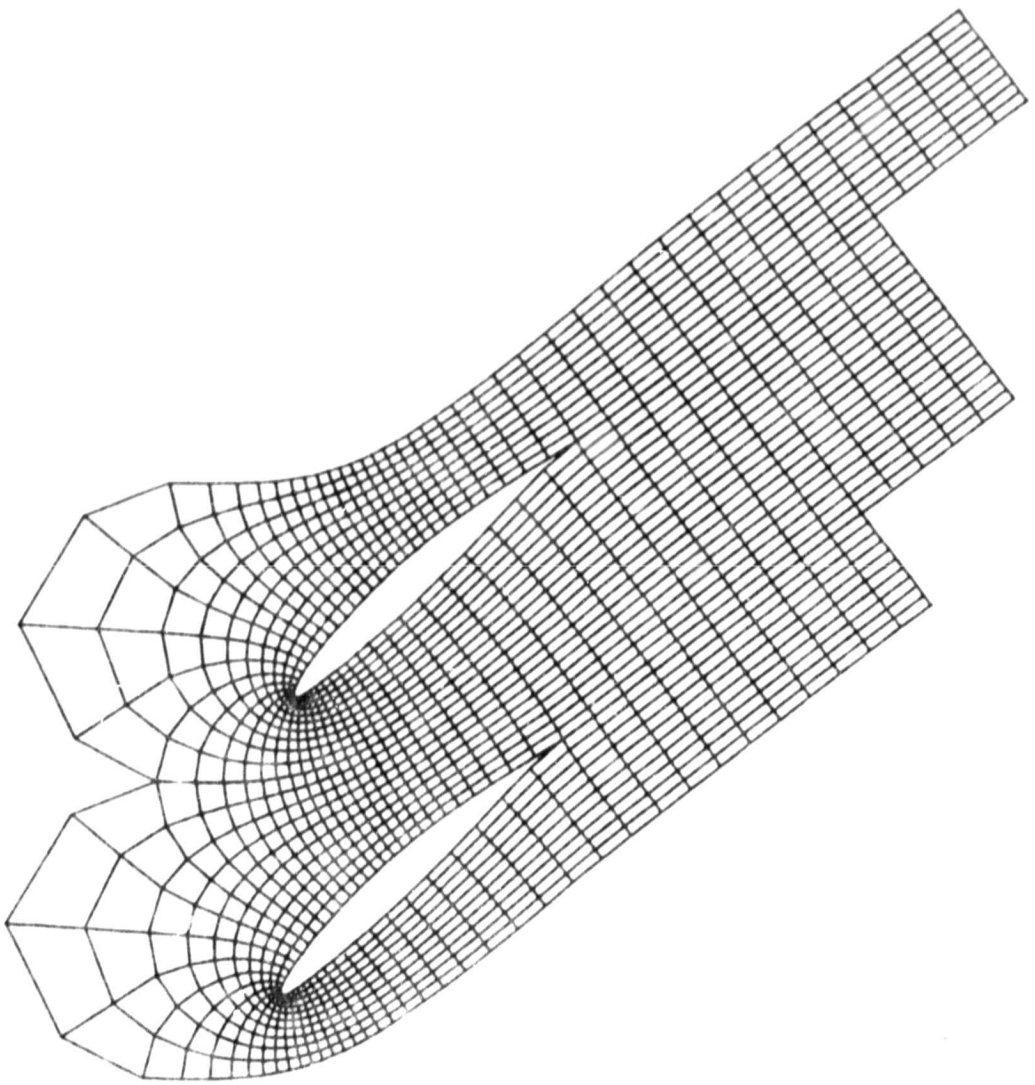

Figure 14. Grid system, 45°staggered cascade (NACA 65-410 blades).

ORIGINAL PAGE IS
OF POOR QUALITY

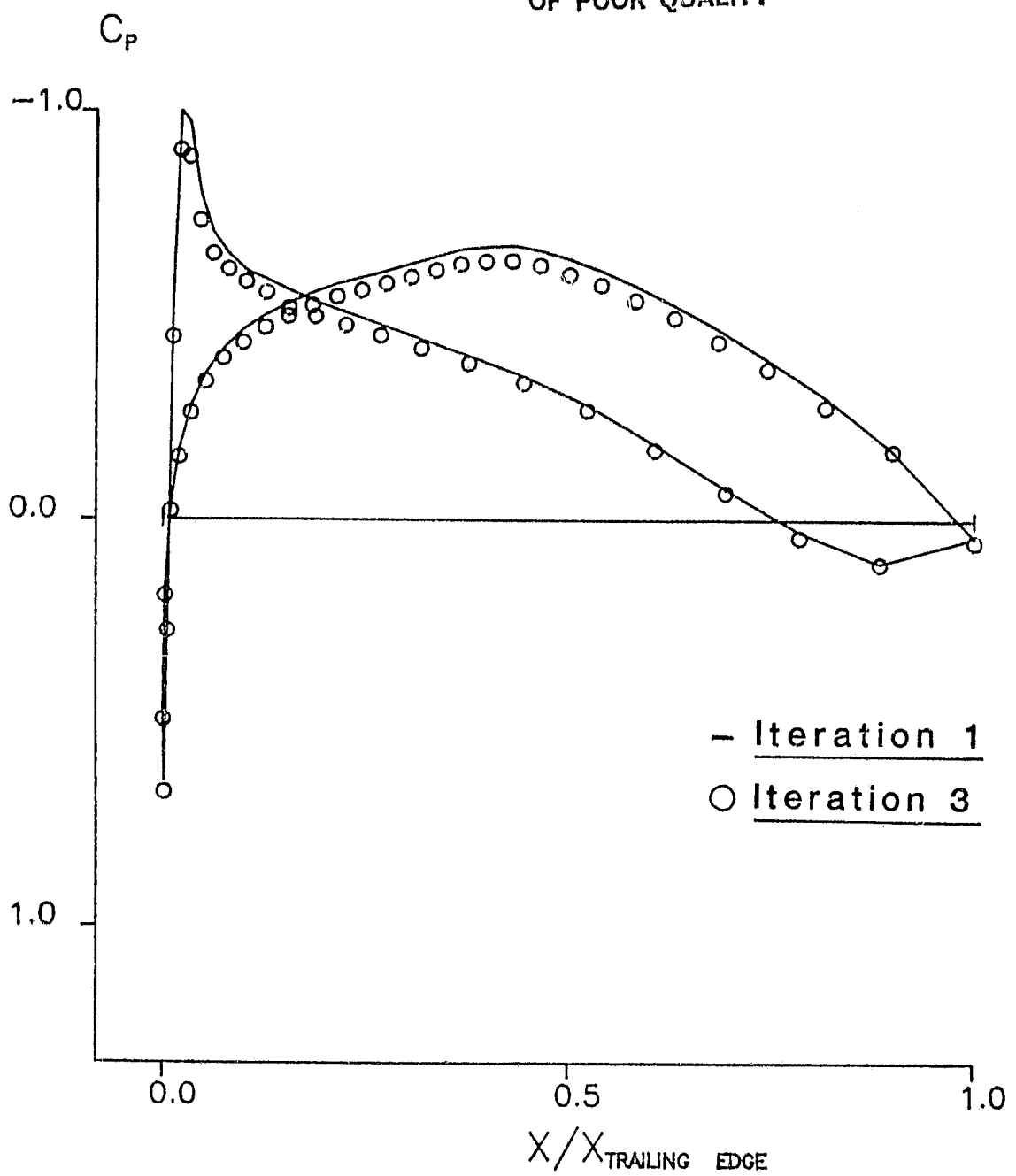

Figure 15. Surface pressure coefficient (NACA 65-410 cascade, $M_{|X=-\infty}$=.47, 3.4° angle of attack).

ORIGINAL PAGE IS
OF POOR QUALITY

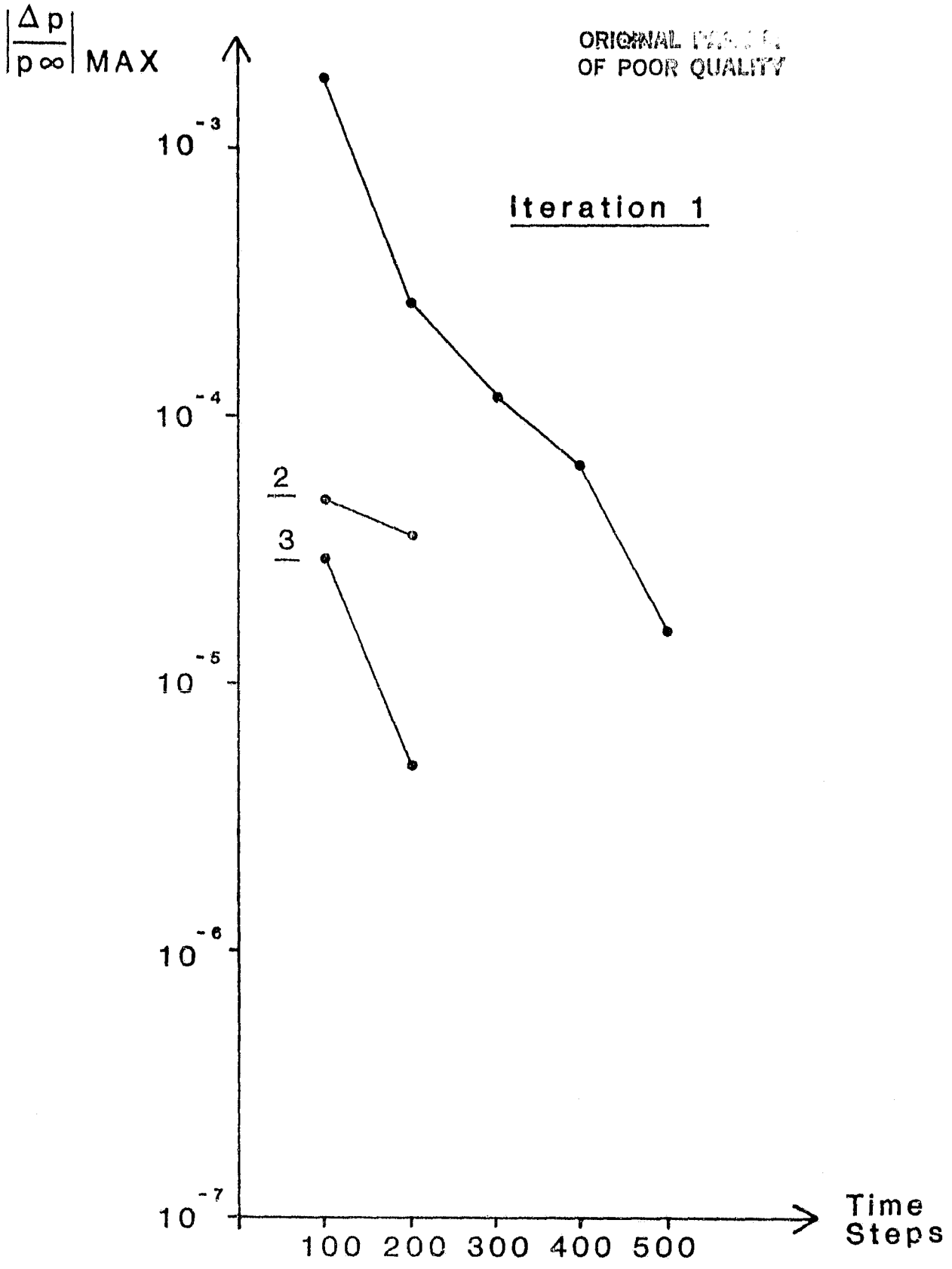

Figure 16. Maximum residual history

ORIGINAL PAGE IS
OF POOR QUALITY

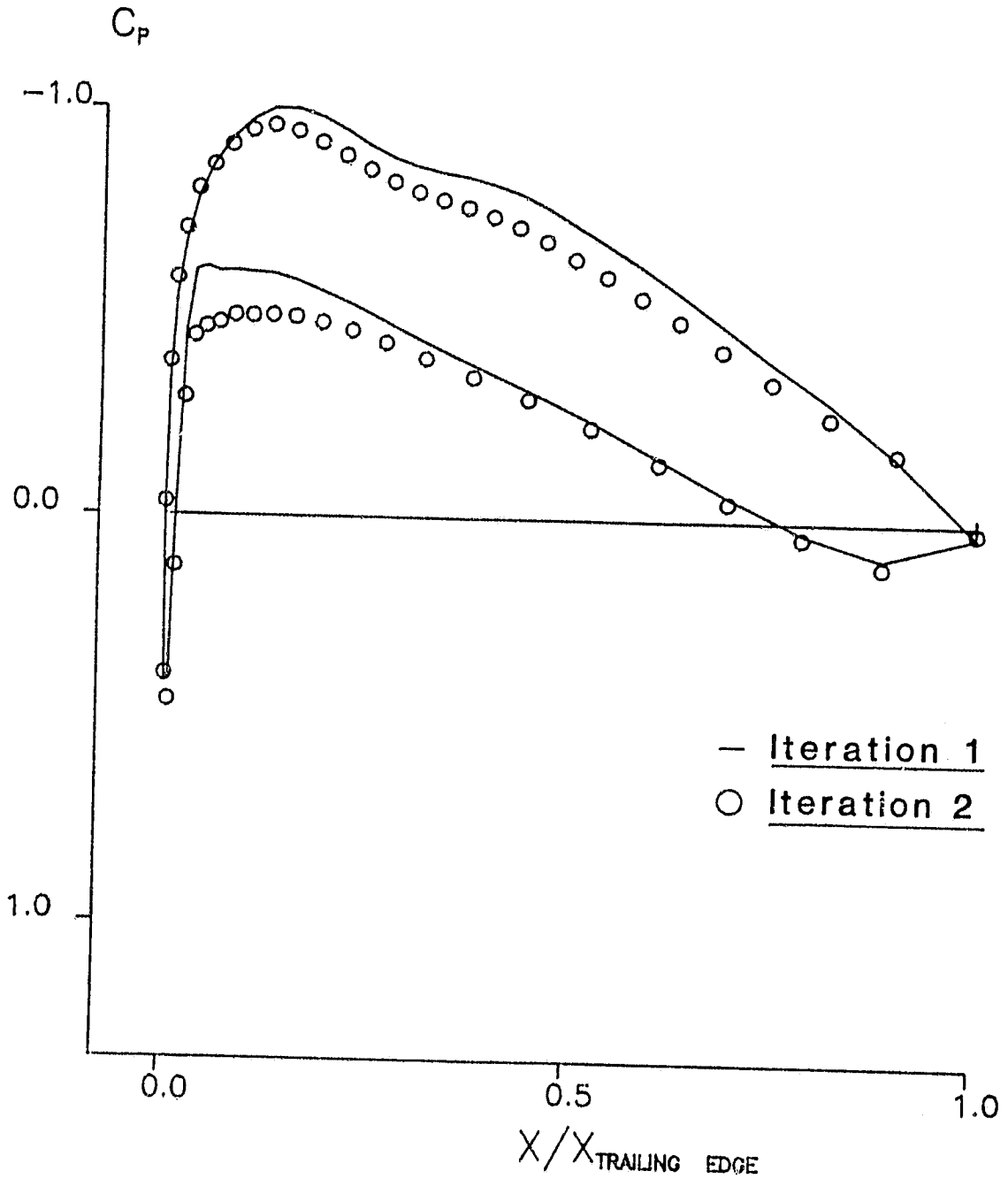

Figure 17. Surface pressure coefficient (NACA 65-410 cascade, $M_{X=-\infty}$=.79, 7.5°angle of attack).

ORIGINAL PAGE IS
OF POOR QUALITY

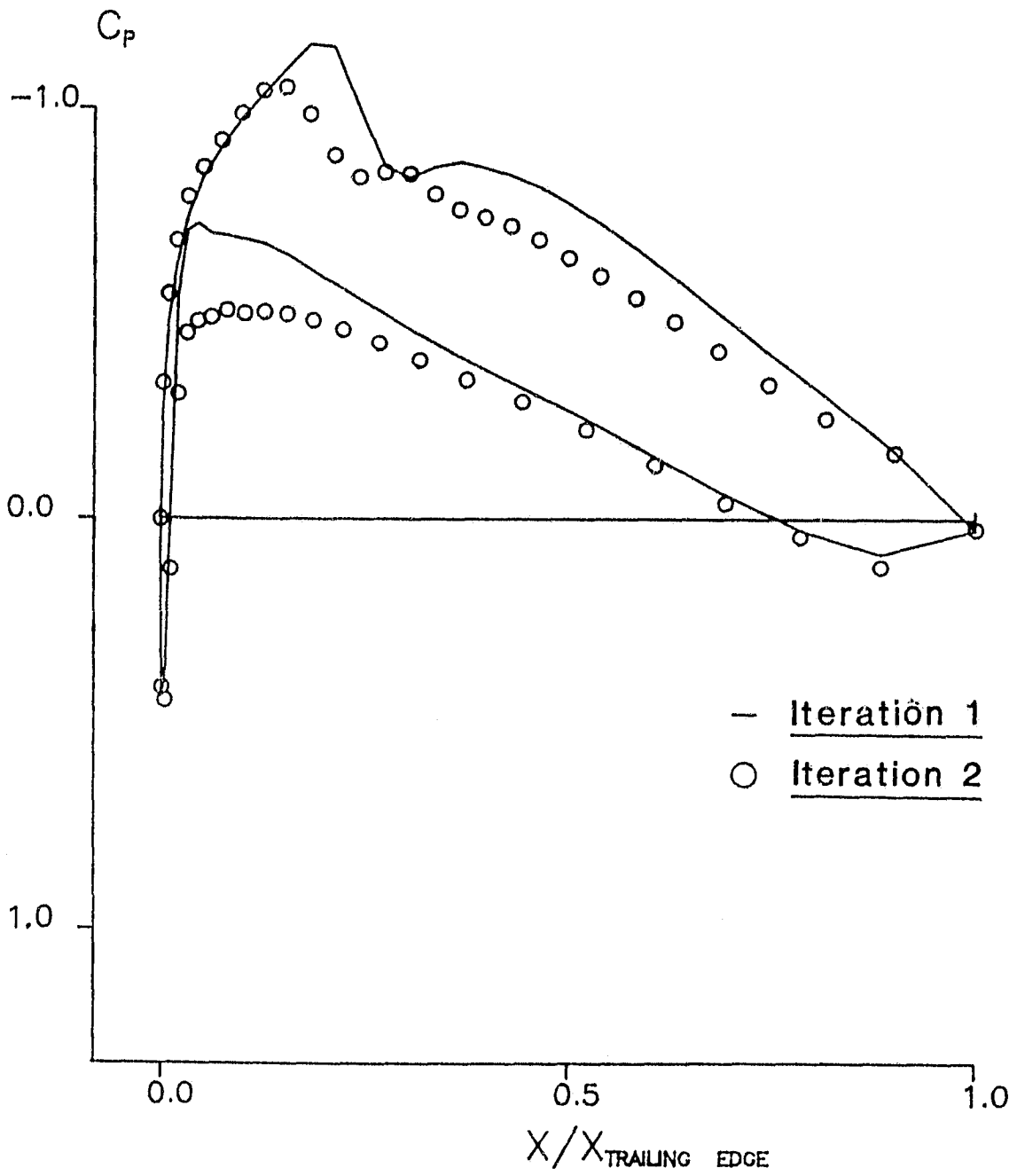

Figure 18. Surface pressure coefficient (NACA 65-410 cascade, $M|_{X=-\infty}=.83$, 7.3° angle of attack).

speed of the flow was also increased so that the flow at the entrance exhibited a Mach number of (.79), and a flow angle of 52.5° (7.5° angle of attack). It may be seen in Figure 17 that the increase in angle of attack has effectively removed the low pressure region on the pressure surface. Also, the figure indicates the presence of an incipient shock on the suction surface at about 25% of chord, due to the increased speed of the flow. This shock is more apparent if the speed of the flow is increased slightly. This has been done in the third test case, where the entering flow had a Mach number of (.83), and a flow angle of 52.3°. As the surface pressure coefficient distribution shown in Figure 18 indicates, a shock has now formed, the location of which is clearly dependent on viscous effects. While convergence tended to be somewhat slower for test cases with the staggered, cambered blade cascade than those with the unstaggered cascade of symmetric blades, nevertheless the interactive calculation procedure was judged to have performed well in all cases considered.

28.5° Staggered Cascade (NACA 65-(12)10 blades)

The success that was experienced in a variety of preliminary test cases prompted the application of the numerical procedure to a cascade situation where a comparison with experiment could be made. The cascade chosen for this purpose consisted of NACA 65-(12)10 blades at a stagger angle of 28.5° and spaced with a gap-chord ratio of (1.0). The grid system used for calculations in this cascade was displayed previously, in a different context, in Figure 5. Comparisons have been made with data collected by Briggs [26] over a range of Mach numbers. In these comparisons we have restricted our attention to the data in [26] which satisfies that author's stated two-dimensionality criterion. The stated

ORIGINAL PAGE IS
OF POOR QUALITY

flow angle in all Briggs' data is 45°, which corresponds to an angle of attack of 16.5°.

A somewhat disappointing result of the numerical calculations carried out on the Briggs cascade, was that a significant boundary layer separation occurred on the suction surface near the trailing edge, which caused the viscous marching solution to fail. This boundary layer separation prevented the execution of viscous-inviscid iterative solutions; consequently, the numerical results presented for the Briggs cascade are strictly inviscid resuts. The inviscid procedure did however perform quite well in these calculations.

We first consider two subsonic test cases with upstream Mach numbers of (.42) and (.61).

Values of the surface pressure coefficient $\left(C_p = \frac{p - p|_{x=-\infty}}{\frac{1}{2}\rho u^2|_{x=-\infty}}\right)$ from the numerical solution and experiment are compared for the $M|_{x=-\infty} = .42$ case, in Figure 19; the agreement apears to be good. Also, the pressure rise predicted by the numerical solution, $\frac{p_\infty}{p|_{x=-\infty}} = 1.055$, agrees well with the experimental value of 1.055. For the $M|_{x=-\infty} = .61$ case, a comparison of surface pressure values in Figure 20 shows fairly good agreement between the numerical solution and experiment. Also, the calculated value for the pressure rise in the cascade of 1.148 agrees fairly well with the experimental value of 1.135.

While the agreement between these two pressure rise values is acceptable, it is not as good as in the $M|_{x=-\infty} = .42$ case, and the comparison deteriorates somewhat further in the transonic case that follows. In that transonic test case, for which additional results will be presented shortly, the apparent overprediction of the pressure rise is still more

ORIGINAL PAGE IS
OF POOR QUALITY

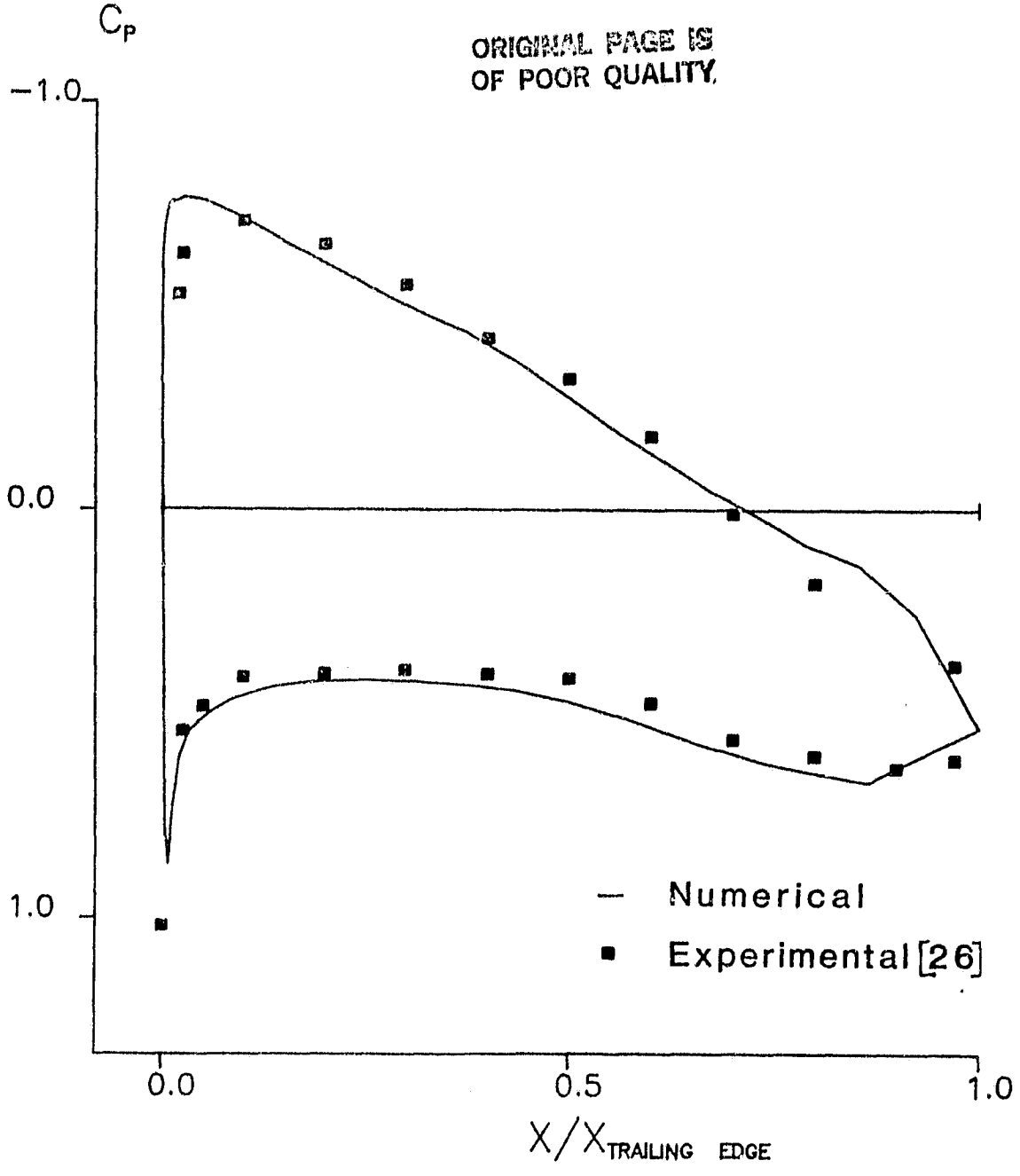

Figure 19. Surface pressure coefficient (Briggs cascade, $M|_{X=-\infty}=.42$).

ORIGINAL PAGE IS
OF POOR QUALITY

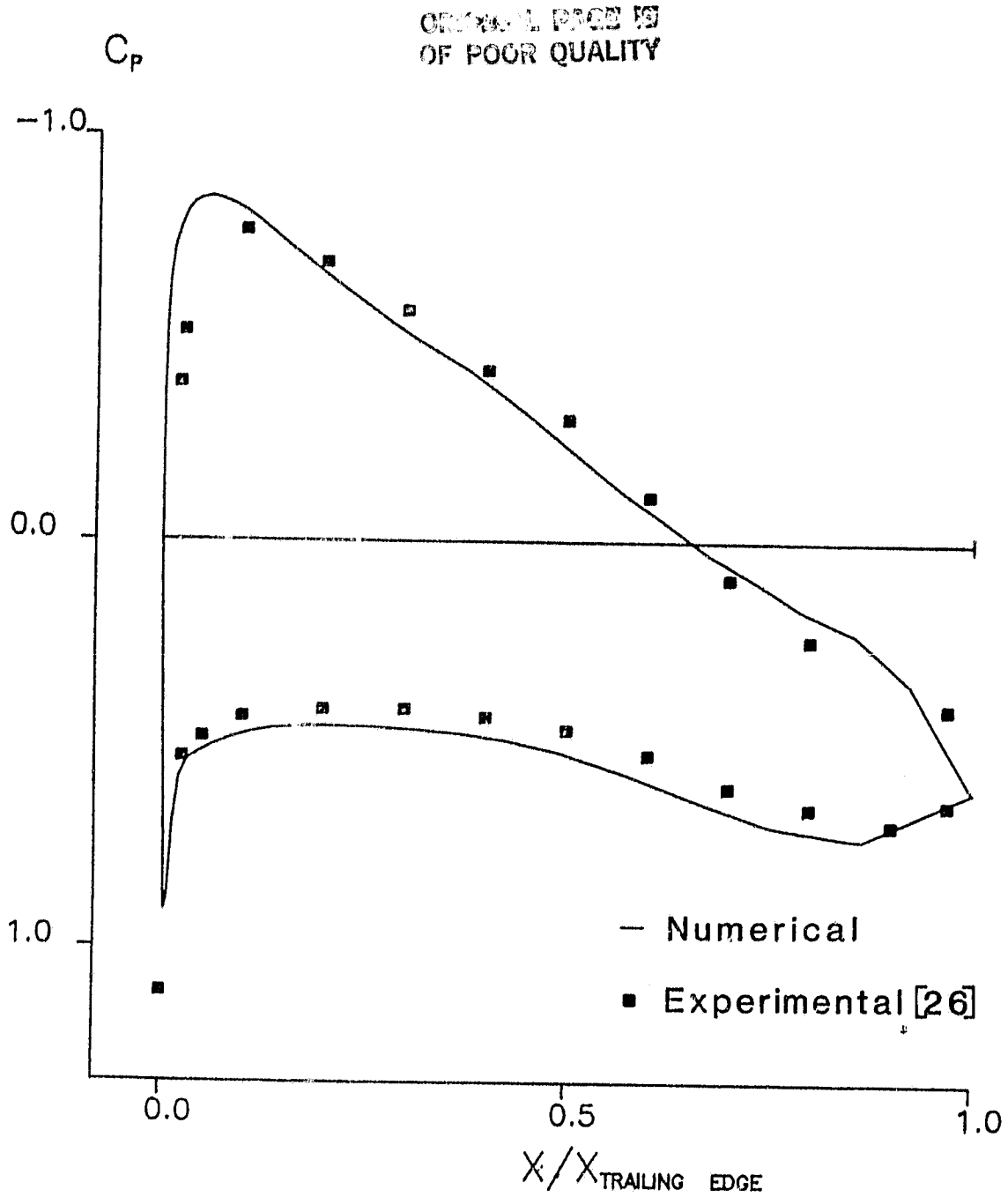

Figure 20. Surface pressure coefficient (Briggs cascade, $M|_{X=-\infty}=.61$).

ORIGINAL PAGE IS
OF POOR QUALITY

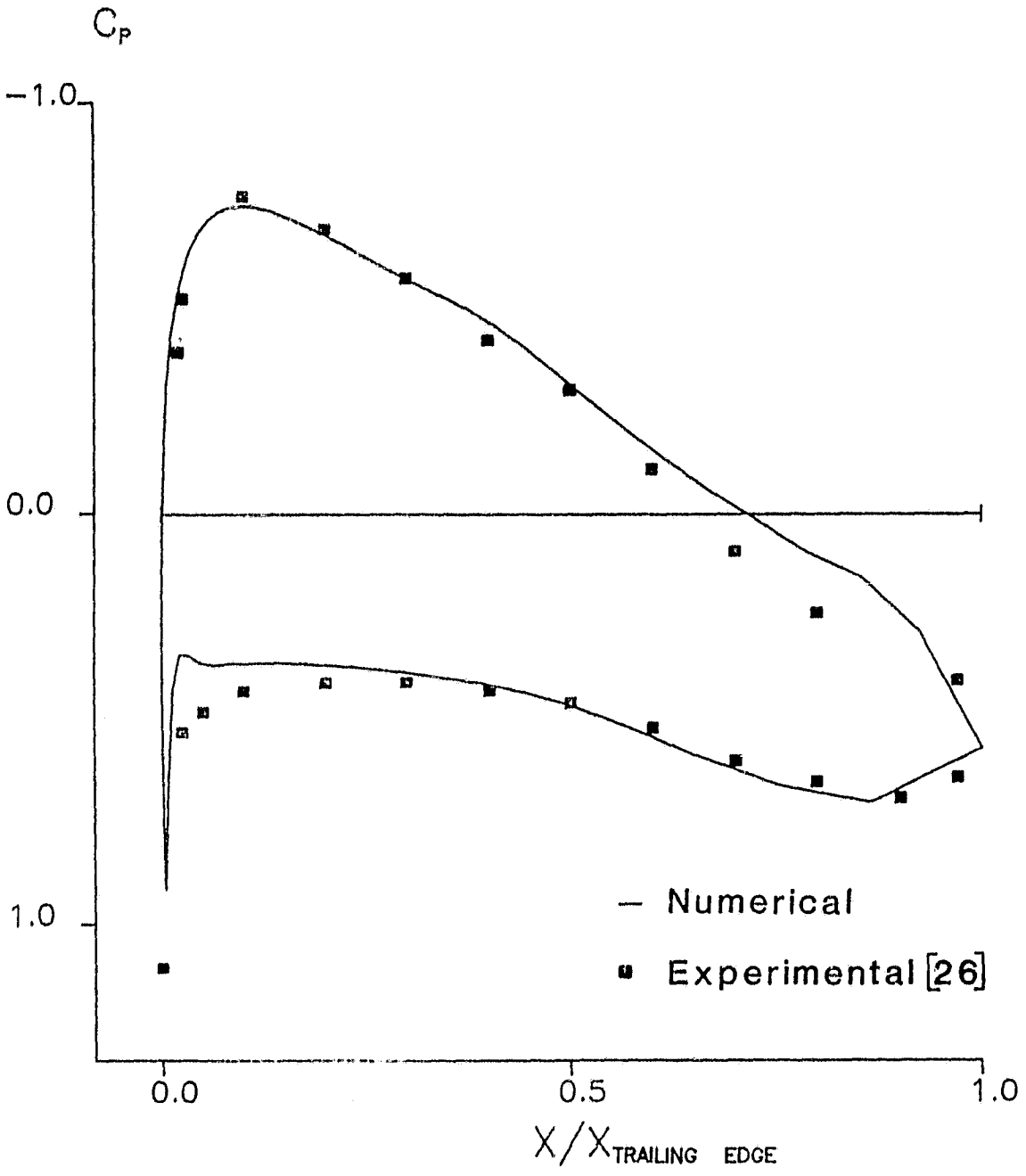

Figure 21. Surface pressure coefficient (Briggs cascade, $M|_{X=-\infty}=.61$, 42.8° flow angle).

severe. It is reasonable to ascribe some of the disparity between the numerical and experimental results to the absence within these numerical solution of any provision for viscous effects. This reasoning is supported both by the fact that the numerical procedure overpredicts the pressure rise, and by the observation that this overprediction tends to worsen with the increase in Mach number. However, our experience with interactive solutions carried out in preliminary test cases indicated that it was unreasonable to attribute all of the overprediction to viscous effects. For this reason, it was resolved to investigate the possibility that the effective angle of attack in the experiment in Reference [26] was slightly less than the stated value. It was also judged a possibliity that the pressure rises recorded in [26] were more reliable data than the flow angle. Our approach then to the investigation of this possiblity was to recalculate the second test case with the 45° flow angle requirement removed and a smaller value of the pressure rise enforced. This recalculation resulted in a Mach number of (.61), but a pressure rise of 1.138 which was closer to the experimental value. The numerical solution gave a value for the upstream flow angle of 42.8° (i.e. a 14.3° angle of attack). The surface pressure coefficient plotted in Figure 21 appears to be in slightly better agreement with the experimental data than the previous numerical solution in Figure 20.

As the final test case wth the Briggs cascade, we have considered a transonic flow situation at an upstream Mach number of (.76), and a flow angle of 45°.

The numerically generated surface pressure coefficient is compared with the experimental data in Figure 22. A value for the cascade pressure

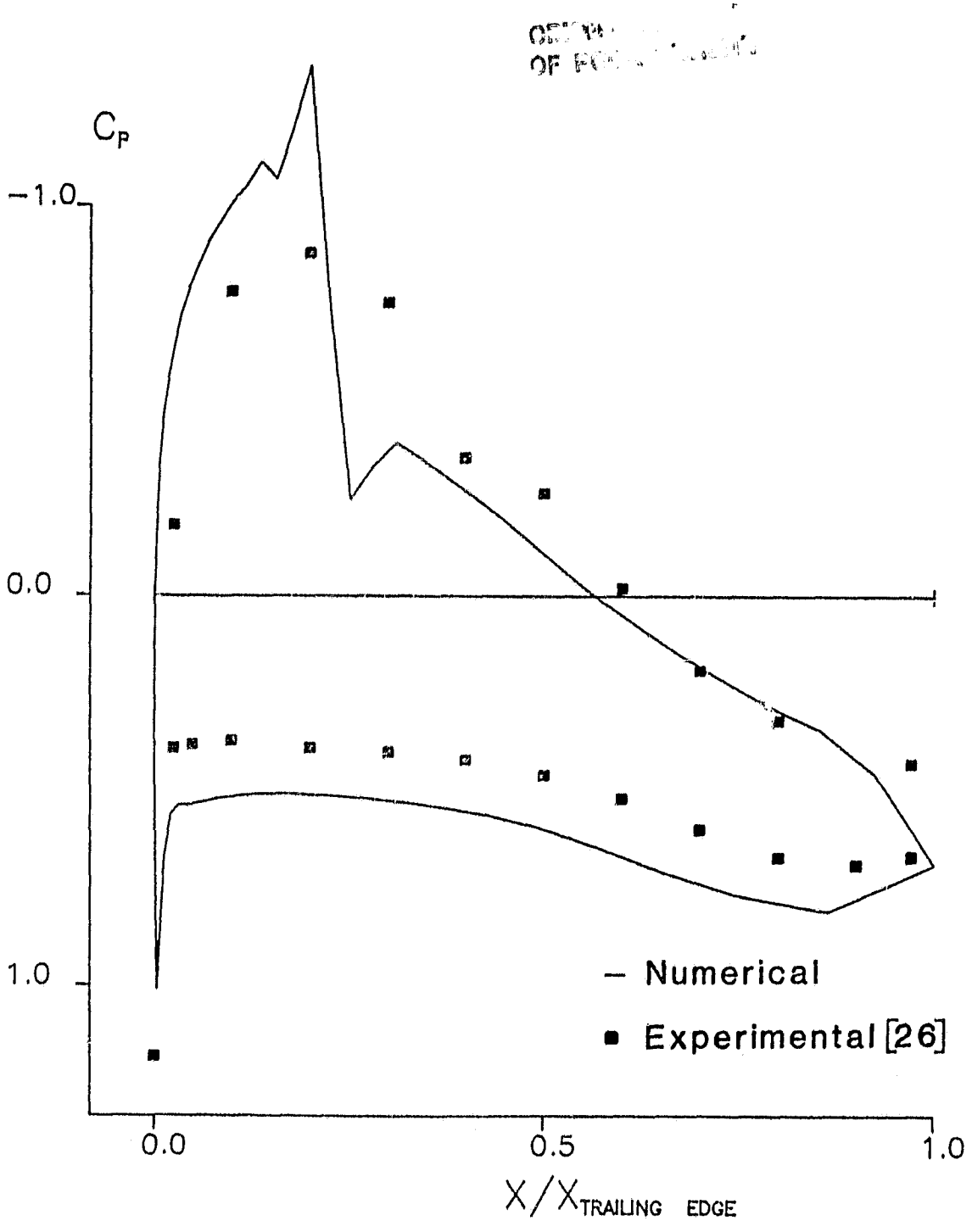

Figure 22. Surface pressure coefficient (Briggs cascade, $M|_{X=-\infty}$=.76).

ORIGINAL PAGE IS
OF POOR QUALITY

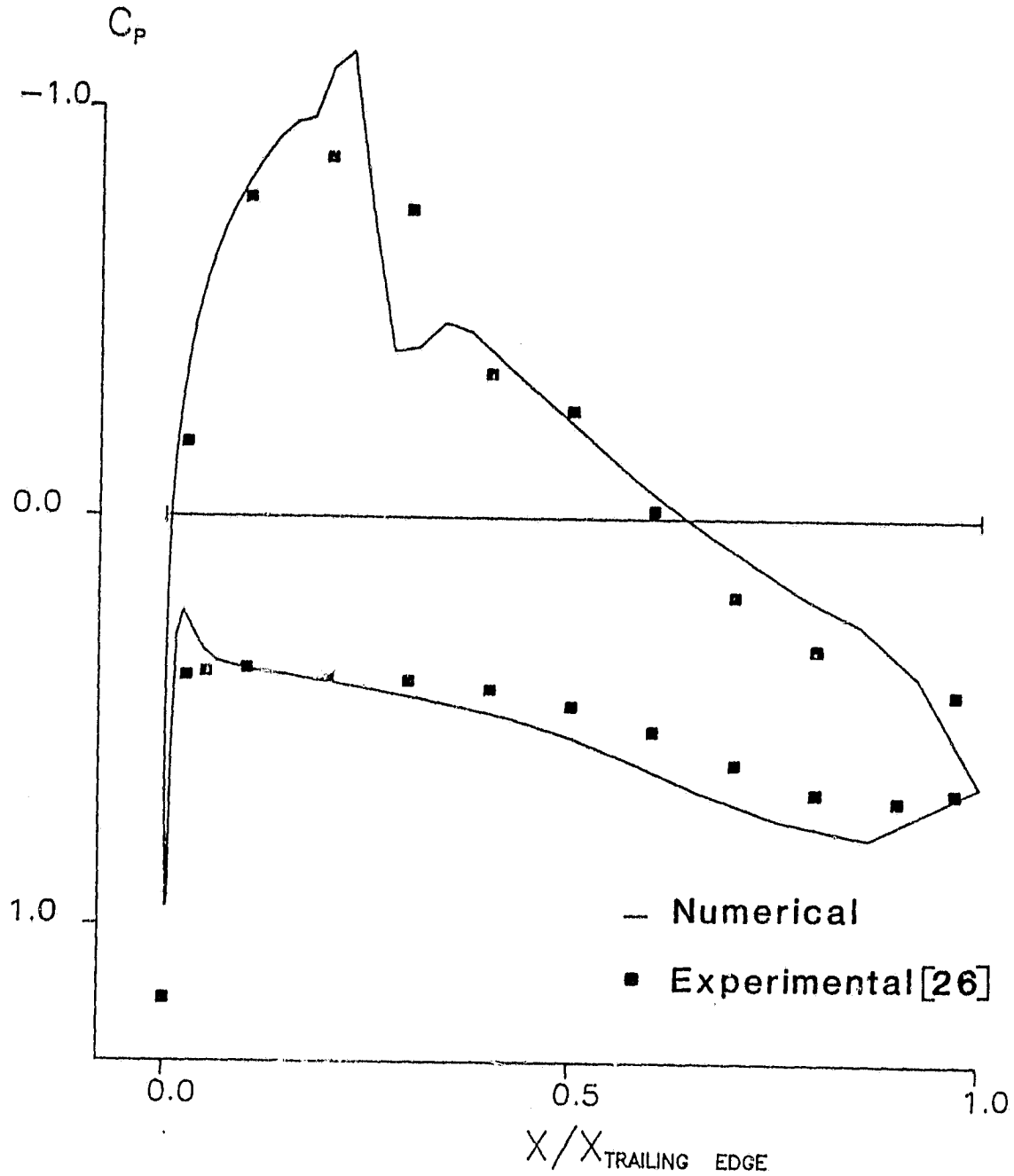

Figure 23. Surface pressure coefficient (Briggs cascade, $M_{|X=-\infty}$=.76, 42.5° flow angle).

ORIGINAL PAGE IS
OF POOR QUALITY

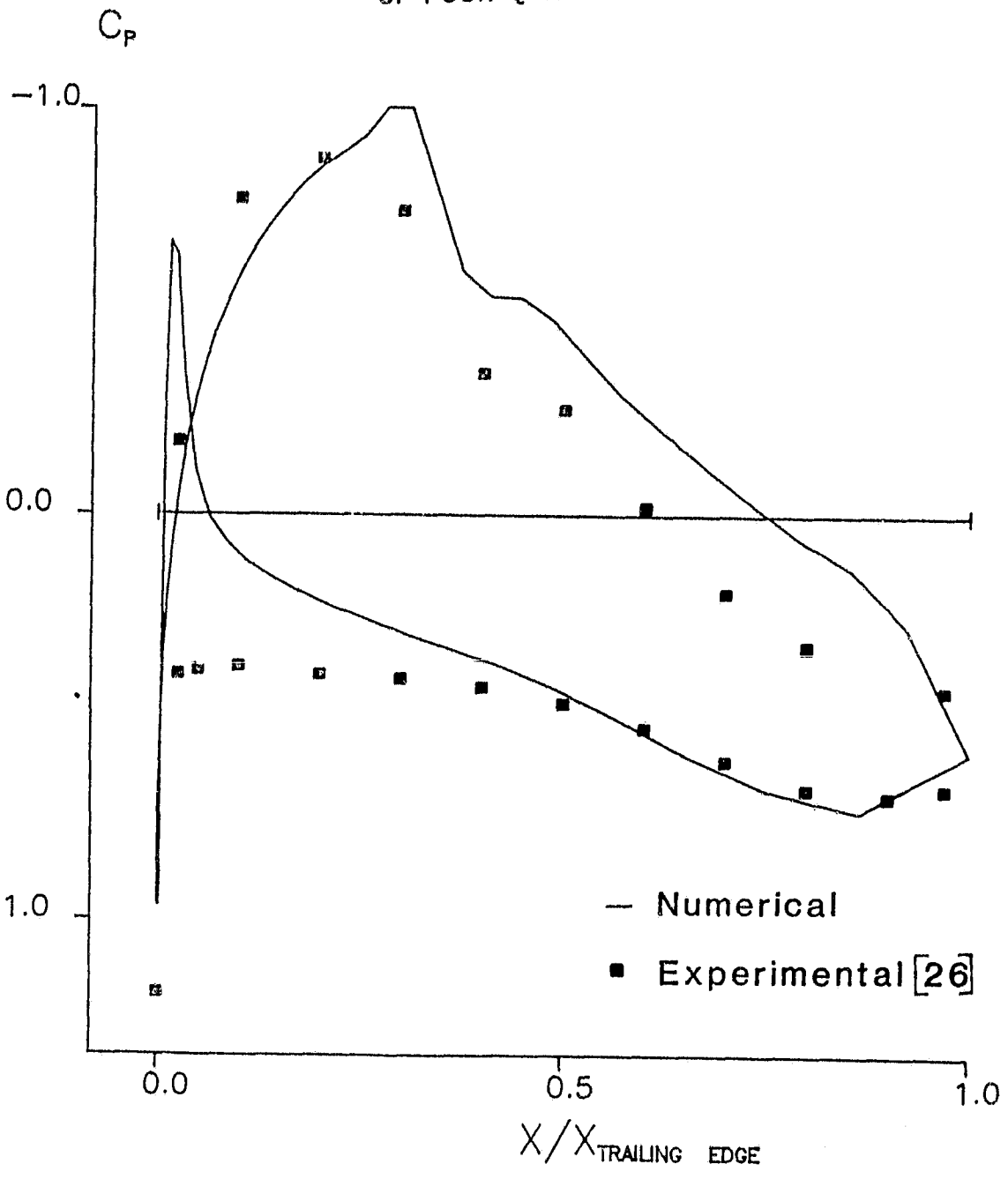

Figure 24. Surface pressure coefficient (Briggs cascade, $M_{X=-\infty}=.76$, 39.2° flow angle).

rise of 1.265 was calculated, the measured value being 1.218. Aside from the shock oscillations in Figure 22, it is clear that the agreement between the numerical and experimental results is not particularly good. The discussion of he shock oscillations is postponed until later. The general lack of agreement in Figure 22 together with the disparity in pressure rise values however, suggested that recalculation of this test case based on a matched pressure increase rather than a matched flow angle, was in order. Since it was unclear as to what portion of the disparity in the pressure increase should be attributed to viscous effects, we have performed two such recalculations at different pressure rise values In the first of these cases a flow with $M|_{x = -\infty} = .76$, and a pressure rise of 1.248, resulted in a flow angle of 42.5° (i.e. a 14° angle of attack). In the second a flow with $M|_{x = -\infty} = .76$, and a pressure rise of 1.217, resulted in a flow angle of 39.2° (i.e. an angle of attack of 10.7°). The numerical results are compared with the experimental data in Figures 23 and 24.

Of the comparisons in Figures 22-24, perhaps the best agreement is in Figure 23, although the agreement in none of these solutions is especially good and the appearance of disagreement is further increased by the spurious shock related wiggles that are present in these plots. In closing the discussion of the present test case, it is noted that the numerically generated pressure coefficient distributions in Figures 22-24 demonstrate that a relatively small change in the angle of attack can cause a large change in results. Since differences in the effective angle of attack of this magnitude might well fall within the bounds of experimental error, the comparisons using matched pressure rises are to be preferred.

Discussion

The numerical results presented here demonstrate the applicability of this numerical calculation procedure to the analysis of flow in cascades. The calculations for which results have been presented required from one to three hours (C.P.U. time) on a CDC Cyber 170/760, where most of the expense was associated with the inviscid solution. Although these run times are large, they were not viewed as prohibitive, particularly since faster computing machines are available. While the method in its present form has been successfully applied to a number of cascade flows, our experience with the method indicates that its range of application could be greatly extended with some modifications. It is our perception that the two most important limitations on the method at present are the shock resolution problems in the inviscid solution, and the failure of the viscous marching solution (and consequently the viscous-inviscid iteration) in situations with significant separation.

The presence of shock induced oscillations in the transonic test cases constitutes the most serious shock related difficulty encountered with the method. These oscillations are prominently displayed in Figure 22, for example. Some standard remedies, which have been applied to this problem in isolated airfoil calculations, proved incapable of relieving the problem for the cascade flows considered here. For example, the attempt to suppress these oscillations by increasing the damping coefficients was frustrated by an apparent stability bound for this calculation of $\epsilon_e < \frac{1}{16}$. Also, an attempt to remove the oscillations by the introduction of "conservative spatial switching", described in Reference [4], and by transitioning the switching operator as described in [4], failed when the

calculation became unstable in the presence of supersonic flow. The failure was somewhat surprising in view of the success experienced with this approach in previous studies [4,8]. In our attempt to resolve the problem in this manner, we have dropped the damping terms in supersonic regions and have in general tried to conform as closely as possible to the prescriptions of [4,8], with the sole exception that we employed a lower order upwind differencing.

Both the failure of the attempt to incorporate "conservative spatial switching" within the method, and the apparent stability bound of $\epsilon_e < \frac{1}{16}$, seemed to indicated that flow in cascades was in some way a more severe test of the inviscid solution algorithm than flow past an isolated airfoil. It is possible that these failures occured because of some incompatibility of the larger damping and the switched differencing with boundary procedures used in the inviscid solution. Also, stability analyses of this algorithm (for example [16]) suggest that more restrictive stability bounds result from the application of periodic boundary conditions, but these analyses do not predict bounds as restrictive as our numerical experience with the present method would indicate. Finally, the possiblity always exists that an error in the coding remained undetected, although it is unlikely that this was the source of the problem. Regardless of the reasons for the failure of these attempts at smoothing the shock oscillations, it is clear that this difficulty must be cvercome for the method to be applied with confidence to shocked flows.

The second important limitation on the method was the failure of the viscous calculation in situations with significant separation. Unlike the difficulty in removing the shock oscillations, this problem was not

unanticipated. The present finite-difference viscous marching solution was chosen for its simplicity, accuracy, and reliability in the treatment of attached boundary layers and wakes. However, it was not expected that this marching solution would accomodate flows that were severely separated. While the viscous marching solution currently employed performed well in a variety of cascade flow situations, the disappointing failure in the Briggs cascade indicated the desirablity of some improvement with regard to separation. As this would likely require the use of an inverse boundary layer procedure, which would then be coupled with the present direct inviscid solution, a viscous-inviscid iterative scheme of the type referred to as "semi-inverse" (see for example [27]) would seem to be required.

In conclusion, it is our opinion that the interactive calculation procedure developed in this study constitutes a useful tool for the analysis of cascade flows which are unshocked and only mildly separated; and with some modification, the generality of the procedure could be increased with regard to these features. The procedure is quite general in terms of cascade geometry and can accomodate a wide range of blade shapes, blade stagger angles, and blade spacings. While a Navier-Stokes approach to the inclusion of viscous effects within the numerical calculation would undoubtedly be required in certain severe flow situations (e.g. massive boundary layer separation with vortex shedding), the viscous-inviscid interactive approach provides an alternative in the analysis of less severe flow situations, such as a cascade operating at or near design conditions. In a time marching solution of the Navier-Stokes equations, it is unlikely that the computational effort expended per grid point would greatly exceed the value for a time marching solution of the Euler equations. However, it

is an advantage of the interactive approach, that this inviscid time marching solution is carried out on a grid that is sparse in comparison with the grid requirements of a Navier-Stokes solution.

REFERENCES

1. MacCormack, Robert W.: The Effect of Viscosity in Hypervelocity Impact Cratering. AIAA Paper No. 69-354, 1969.

2. Briley, W. R. and McDonald, H.: An Implicit Numerical Method for the Multidimensional Compressible Navier-Stokes Equations. United Aircraft Research Laboratories Report M911363-6, Nov. 1973.

3. Beam, Richard M. and Warming, R. F.: An Implicit Finite-Difference Algorithm for Hyperbolic Systems in Conservation Law Form. J. of Comp. Phys., Vol. 22, No. 1, pp. 87-110, 1976.

4. Beam, Richard M. and Warming, R. F.: An Implicit Factored Scheme for the Compressible Navier-Stokes Equations. AIAA Journal, Vol. 16, No. 4, pp. 393-402, April 1978.

5. MacCormack, Robert W.: An Efficient Numerical Method for Solving the Time-Dependent Compressible Navier-Stokes Equations at High Reynolds Number. Paper presented at the ASME 97th Winter Annual Meeting, New York, Dec. 5-10, 1976.

6. Thompson, J. F., Thames, F. C. and Mastin, C. M.: Automatic Numerical Generation of Body-Fitted Curvilinear Coordinate System for Field Containing Any Number of Arbitrary Two-Dimensional Bodies. J. of Comp. Phys. Vol. 15, No. 3, pp. 299-319, 1974.

7. Thames, F. C., Thompson, J. F., and Mastin, C.M.: Numerical Solution of the Navier-Stokes Equations for Arbitrary Two-Dimensional Airfoils. NASA SP-347, Pt. 1, pp. 469-530, 1975.

8. Steger, J. L.: Implicit Finite Difference Simulation of Flow about Arbitrary Two-Dimensional Geometries. AIAA Journal, Vol. 16, No. 7, pp. 679-686, July 1978.

9. Ives, D. C., and Liutermoza, J. G.: Analysis of Transonic Cascade Flow Using Conformal Mapping and Relaxation Techniques. AIAA Journal, Vol. 15, No. 5, pp. 647-652, May 1977.

10. Ghia, U. and Ghia, K. N.: Numerical Generation of a System of Curvilinear Coordinates for Turbine Cascade Flow Analysis. Report No. AFL 75-4-17, University of Cincinnati, 1975.

11. Eiseman, P. R.: A Coordinate System for a Viscous Transonic Cascade Analysis. J. of Comp. Phys., Vol. 26, pp. 307-338, 1978.

12. Adamczyk, J.: An Electrostatic Analogy for Generating Cascade Grids. NASA Conference Publication No. 2166, 1980.

13. Steger, J. L., Pulliam, T. H., and Chima, R. V.: An Implicit Finite Difference Code for Inviscid and Viscous Cascade Flow. AIAA Paper No. 80-1427, 1980.

14. Kober, H.: Dictionary of Conformal Representations, Second Edition with corrections, Dover Publications, 1957.

15. Varga, R. S.: Matrix Iterative Analysis, Prentice-Hall, 1962.

16. Desideri, J. A., Steger, J. L. and Tannehill, J. C.: On Improving the Iterative Convergence Properties of an Implicit Approximate Factorization Finite Difference Algorithm, NASA TM 78495, June 1978.

17. Rudy, D. H. and Strikwerda, J. C.: A Nonreflecting Outflow Boundary Condition for Subsonic Navier-Stokes Calculations. J. of Comp. Phys., Vol. 36, pp. 55-70, 1980.

18. Moretti, Gino: The Choice of A Time-Dependent Technique in Gas Dynamics. PIBAL Report No. 69-26, Polytechnic Institute of Brooklyn July 1969.

19. Cebeci, T., and Smith, A.M.O.: Analysis of Turbulent Boundary Layers, Academic Press, 1974.

20. Chen, K. K., and Thyson, N. A.: Extension of Emmons Spot Theory to Flows on Blunt Bodies. AIAA Journal, Vol. 9, No. 5, pp. 821-825, May 1971.

21. Cebeci, T., Thiele, F., Williams, P. G., and Stewartson, K.: On the Calculation of Symmetric Wakes I. Two-Dimensional Flows. Numerical Heat Transfer, Vol. 2, pp. 35-60, 1979.

22. Schlichting, H.: Boundary Layer Theory, Sixth Edition, McGraw-Hill, 1968.

23. Hornbeck, R. W.: Numerical Marching Techniques for Fluid Flows with Heat Transfer, NASA SP-297, 1973.

24. Johnston, W., and Sockol, P. and Reshotko, E.: A Viscous-Inviscid Interactive Compressor Calculation. Report No. FTAS TR-78-136, Case Western Reserve University, 1978.

25. Rehyner, T. A. and Flugge-Lotz, I.: The Interaction of a Shock Wave with a Laminar Boundary Layer. Int. J. of Non-Linear Mech., Vol. 3, pp. 173-199, 1968.

26. Briggs, W. B.: Effect of Mach Number on the Flow and Application of Compressibility Corrections in a Two-Dimensional Subsonic Transonic Compressor Cascade Having Varied Porous-Wall Suction at the Blade Tips. NACA TN 2649, 1952.

27. Wigton, L. B., and Holt, M.: Viscous Inviscid Interaction in Transonic Flow. AIAA Paper No. 81-1003, 1981.